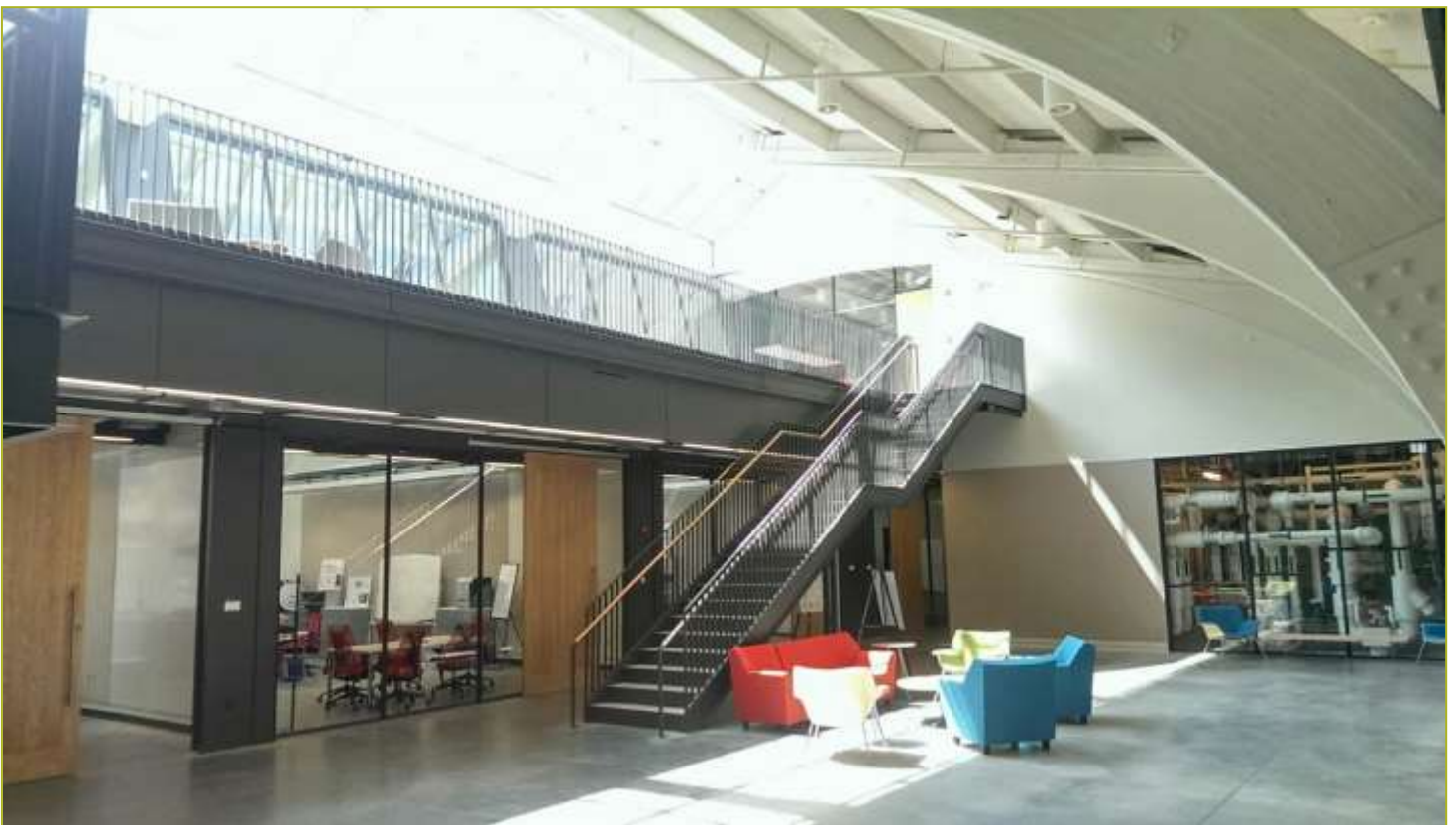


Title: Voltron Compatible Virtual Sensor FDD System for
Roof Top Units

Report Date: April 29, 2016

Report Author: Andrew L. Hjortland, James E. Braun



Report Abstract

Project Objectives

- Build on BP4 evaluation and testing of cost-effective virtual sensor based RTU diagnostics with a focus on overall performance degradation (COP, capacity).
- Apply developed methodology and demonstrate implementation within VOLTTRON in the laboratory including on-line estimation of the impacts of faults on performance and operating costs to determining when service should be performed.

A fault detection and diagnostics system for rooftop air conditioners was developed using low-cost electronics. The system was designed to be compatible with the VOLTTRON™ monitoring and control platform. The underlying fault detection and diagnostics methodology implemented in the system utilizes virtual sensors to measure parts of the equipment operation that are sensitive to common faults. Using virtual sensors reduces costs while also providing accurate and reliable diagnostics.

The electronics hardware and FDD software are described in this report and a link to the publically available software repository has been included. Each component of the system has been described in this report along with a discussion of the design choices. Finally, the system was tested using data collected for four different rooftop unit configurations in a laboratory setting. The rooftop units were tested under a large range of operating conditions and combinations of improper refrigerant charge levels, condenser fouling levels, and evaporator fouling levels.

Contact Information for lead researcher

Name: James E. Braun

Institution: Purdue University

Email address: jbraun@purdue.edu

Phone number: 765-494-9157

Contributors

Andrew L. Hjortland, Orkan Kurtulus, James E. Braun – Purdue University



1 Introduction

1.1 RTU AFDD Background

Studies have shown that packaged commercial rooftop unit (RTU) air conditioning equipment tend to be poorly maintained and significant energy may be wasted due to unnoticed or unrepaired equipment faults. One often cited review of FDD technologies for building systems estimates between 10-30% additional annual energy may be caused by repairable faults (Katipamula and Brambley 2005). While uncertainty about the prevalence of different faults still exists, previous field studies have shown that RTUs may benefit from automated FDD (Jacobs 2003; Cowan 2004, Li and Braun 2007). Previous work on FDD for HVAC systems has yielded positive results and shown potential for significant energy and utility cost savings through early identification of faults.

However, manufacturers have been slow to incorporate FDD technologies for a few reasons:

- FDD systems must be low-cost and easy to install,
- uncertainty with respect to economic benefit/savings potential still exists,
- and lack of integration and interoperability with other building technologies.

In order to address these issues, a complete automated FDD system has been designed that implements a previously developed automated FDD system using virtual sensors (Li and Braun 2007, 2009). The system is able to monitor operation of an RTU continuously and detect and diagnose multiple faults that may be affect the system simultaneously. In addition, a methodology to estimate the total impact on equipment performance has been implemented using the virtual sensors and reference models that estimate normal performance.

What follows is a technical description of the FDD system that has been developed for RTUs. The remainder of this section gives a high level overview of the system architecture and the open-source monitoring and control platform utilized to implement the system in software. In Section 2, a description of the low-cost system hardware is presented, including an initial estimate of the component costs. In Section 3, a high level description of the automated FDD algorithms is presented, along with references to the original work for more details. In Section 4, results collected from applying the system to a system in a laboratory setting are presented. Finally, in Section 5, the completed work is summarized and possible future work is proposed.

1.2 Overview of AFDD Architecture

Two hurdles that limit the adoption of FDD in existing RTUs and most new RTUs are the lack of installed sensors and peripheral communications. Without these two pieces, it is both difficult to detect problems due to minimal available information and to alert building owners and facility managers about problems in a timely and effective manner. With this in mind, a dedicated FDD module has been developed that can be integrated within or in parallel with existing RTU controllers. The system addresses the need for sensors by integrating measurement circuits and can utilize existing internet



infrastructure for communications. A schematic outline of the system architecture in relation to existing RTU controllers is shown in Figure 1.1.

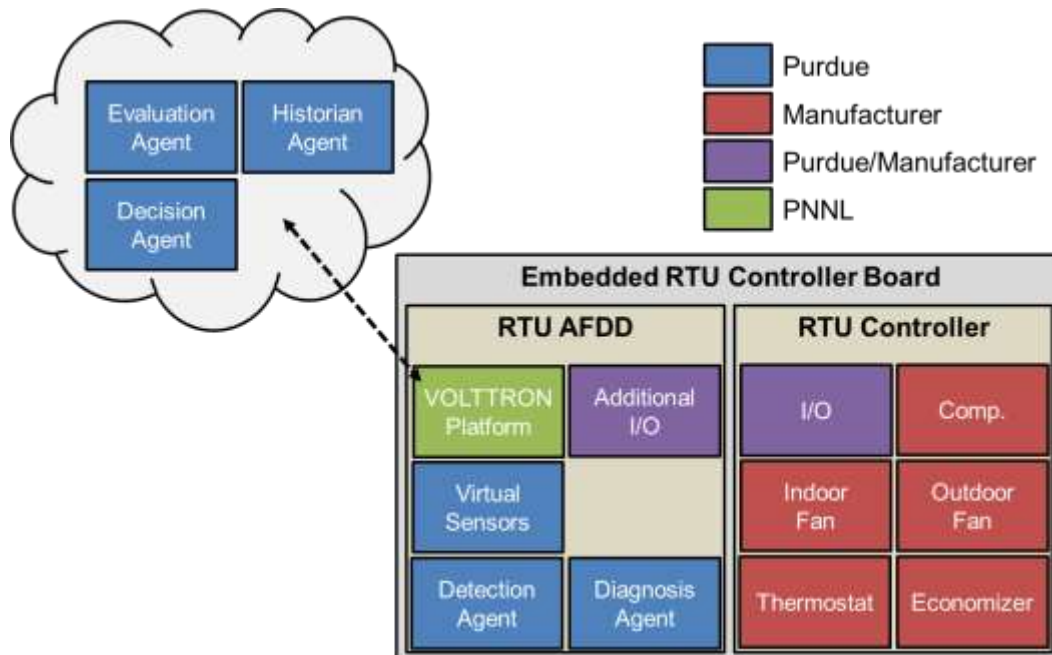


Figure 1.1. Overall architecture of VOLTRON enabled RTU AFDD system as an additional module of current RTU control units.

It should be noted that integrating a dedicated FDD module in existing RTU controllers is not the only possible solution for detecting and diagnosing equipment faults. An alternative solution, commonly called in-field FDD, uses devices that can be temporarily installed on equipment to aid field technicians in determining problems. A significant advantage of these diagnostics tools is that the cost can be distributed to many different RTUs since they can be generally applied. However, designing a tool that can be generally applied to many different RTUs while still having sufficient fault detection sensitivity and false alarm rejection is challenging (Yuill and Braun 2013). In addition, in-field FDD requires inspection of actual RTUs in order to detect and diagnose faults but previous studies have concluded that RTU inspection may be infrequent (Jacobs 2003; Cowan 2004; NMR Group 2015). Finally, the cost of sending service technicians into the field is significant in comparison with monitoring the health of equipment using electronics.

From its conception, the automated FDD (AFDD) system has been developed with the potential for existing as a standalone system within the RTU controller. This means it was essential to incorporate all basic components of an AFDD product: a sensor measurement and data acquisition (DAQ) module, a fault detection module, and a fault diagnosis module. While this involved some hardware design, extensive software development was required to incorporate the AFDD methods and algorithms. Rather than using propriety tools and code, the RTU AFDD system leverages open-source software exclusively, most importantly the VOLTRON™ monitoring and control platform (Somasundaram et al



2014, Akyol et al 2015). The VOLTTRON™ platform, developed by the US Department of Energy, facilitates communication between software agents and other physical devices and resources with a primary focus on building systems and technologies. The role of VOLTTRON™ plays in the RTU AFDD system is to act as a message broker between AFDD services so that development, operation, and management may be organized hierarchically. This modularity offers the flexibility to modify, add, or completely swap out individual subcomponents depending on system requirements.

Many automated FDD approaches have been previously proposed for RTUs (Rossi and Braun 1996; Armstrong et al 2006; Li and Braun 2007; Najafi et al 2012; Katipamula et al 2015; Hjortland and Braun 2016). The system described in this work implements a virtual sensor based methodology originally described by Li and Braun (2007). One major advantage of the virtual sensor approach is the ability to diagnose faults in the presence of multiple simultaneous faults. This is important since many faults may contribute to degradations in system performance over time. Using virtual sensors, the impacts on cooling capacity and efficiency of these degradations can be estimated systematically. Using these impact estimates, more sensible maintenance and service decisions can be made.



2 Description of AFDD Hardware

Due to the limited availability of sensors installed on existing RTUs in production and the relatively modest computing resources available, additional electronics hardware is required to implement the RTU AFDD methodology proposed in this work. The following section details the electronics designed to demonstrate the complete performance of the RTU AFDD system: from data acquisition to fault detection and diagnostics and finally fault impact evaluation. The system designed can be considered standalone. These electronics can be installed on a typical RTU and with the proper initial configuration, an effective AFDD system can be utilized by building operators without any other sensor requirements or hardware. While this system could seemingly be applied as a retrofit, it was primarily designed from the standpoint of being embedded by equipment manufacturers during the production process.

2.1 Data Acquisition and Compute System

2.1.1 Sensor Inputs

In order to implement the virtual-sensor-based AFDD algorithms, several refrigerant-side temperature measurements (shown in Table 2.1) are required. Using only these refrigerant-side temperature sensors several of the virtual sensors can be implemented, including the virtual refrigerant charge (VRC) sensor, the virtual refrigerant mass flow rate (VRMF) sensor, the virtual compressor power (VCP) sensor, the virtual cooling capacity sensor, and the virtual COP sensor. To measure these refrigerant-side temperatures, a low-cost buffered analog-to-digital thermistor circuit was designed. The thermistors selected for the application can be easily surface-mounted to the RTU refrigerant circuit in the locations required. In comparison to other types of temperature sensors (thermocouples, RTDs, etc.) thermistors offer a good combination of accuracy, reliability, and cost. When using thermistors, the highly nonlinear relationship between temperature and internal resistance must be considered during the design process. While there are different ways to address this problem, each with their own tradeoffs, a more expensive (yet still relatively inexpensive) analog-to-digital converter (ADC) with a higher resolution was selected for this application.

Table 2.1. Description of required refrigerant-side temperature sensors used for RTU AFDD methods.

Symbol	Type	Description
T_{eri}	10 k Ω Thermistor ¹	Evaporator Refrigerant Inlet Temperature
T_{suc}	10 k Ω Thermistor	Compressor Refrigerant Suction Temperature
T_{dis}	10 k Ω Thermistor	Compressor Refrigerant Discharge Temperature
T_{crs}	10 k Ω Thermistor ²	Condenser Refrigerant Saturation Temperature
T_{cro}	10 k Ω Thermistor	Condenser Refrigerant Outlet Temperature

¹ In some applications, a compressor suction pressure measurement is available. When this is the case, the T_{eri} sensor is not required since the evaporating temperature can be calculated using two-phase property relations.

² In some applications, a compressor discharge pressure measurement is available. When this is the case, the T_{crs} sensor is not required since the condensing temperature can be calculated using two-phase property relations.



It should also be noted that pressure measurements can be used to calculate the evaporator refrigerant inlet temperature and condenser refrigerant saturation temperature since the refrigerant at these points is a two-phase fluid. When this is the case, the saturation temperature and pressure are not independent with their relationship determined by an equation of state. Systems that already have these pressure sensors installed for control purposes do not need to install additional temperature sensors which reduces the additional instrumentation costs for AFDD. It is also worth noting that pressure sensors may be required for systems with micro-channel condensers. Locating a consistent and reliable saturation temperature point over the expected equipment operating range is not trivial task.

In order to determine whether the condenser coil has been fouled or some other airflow restriction has occurred, the RTU AFDD system uses a virtual condenser airflow (VCAF) sensor. This virtual sensor requires two additional air-side temperature sensors to measure the entering and leaving condenser air temperatures (described in Table 2.2). In the designed prototype, thermistor measurement circuits identical to the refrigerant-side measurements were use. This offered a more consistent design and provided the same advantages previously stated. One additional consideration that is required of the air-side measurements is to ensure that the thermistor probes were properly insulated from nearby surfaces so that accurate air temperatures were measured. This was not an issue for the refrigerant-side temperature sensors since they were mounted on the refrigerant piping and insulated from the surroundings.

Table 2.2. Description of the required air temperature sensors used in the virtual condenser airflow sensor.

Symbol	Type	Description
T_{cai}	10 k Ω Thermistor	Condenser Air Inlet Temperature
T_{cao}	10 k Ω Thermistor	Condenser Air Outlet Temperature

The RTU AFDD methodology requires a calculation of the enthalpy of the entering and leaving evaporator air in order to determine if the evaporator coil is fouled. Measuring enthalpy directly is not possible, so the temperature and relative humidity at these points is measured instead. A description of these sensors is shown in Table 2.3. In the initial design, two solid-state sensors that measured both the dry-bulb temperature and relative humidity were used. Unlike the analog thermistor circuits described previously, these sensors provide a digital output using the I²C communications protocol. Besides using these sensors for the virtual evaporator airflow (VEAF) sensor, the entering evaporator air drybulb temperature and wetbulb temperature is used as inputs in reference models of normal performance also used by the AFDD algorithms.

Table 2.3. Description of the required air temperature and relative humidity sensors used in the virtual evaporator airflow sensor for systems without economizers.

Symbol	Type	Description
T_{eai}	Temp/RH Chip	Evaporator Air Inlet Temperature
ϕ_{eai}	Temp/RH Chip	Evaporator Air Inlet Relative Humidity
T_{eao}	Temp/RH Chip	Evaporator Air Outlet Temperature
ϕ_{eao}	Temp/RH Chip	Evaporator Air Outlet Relative Humidity



Compared to the other virtual sensors, the number of sensors required for the virtual evaporator airflow rate sensor is relatively large and costly. Recently, some RTU equipment manufacturers have announced evaporator airflow rate virtual sensors estimated using alternative methodologies. One manufacturer has also integrated this technology with an economizer to provide estimations of both supply airflow rate and ventilation airflow rate (Lennox Commercial, 2015). Integration with this system would eliminate the need for some of the sensors described in Table 2.3, though the entering evaporator air condition is still needed to evaluate the system performance reference models.

For RTUs with airside economizers, accurately measuring the entering evaporator air (mixed air) temperature using a single-point sensor is very difficult due to poor mixing within the mixing box. Some methodologies use the outdoor air and return air measurements along with information about the damper position to correct this measurement. Depending on the type of economizer control used, additional drybulb temperature and relative humidity sensors measuring the outdoor air and return air condition may be available for AFDD. In order to handle these sensors, arrangements were made on the initial DAQ prototype design to handle additional analog or digital sensor inputs. A description of these additional sensors for systems with economizers is shown in Table 2.4.

Table 2.4. Description of the required air temperature and relative humidity sensors used in the virtual evaporator airflow sensor for systems with economizers.

Symbol	Type	Description
T_{ra}	Temp/RH Chip	Return Air Temperature
ϕ_{ra}	Temp/RH Chip	Return Air Relative Humidity
T_{oa}	Temp/RH Chip	Outdoor Air Temperature
ϕ_{oa}	Temp/RH Chip	Outdoor Air Relative Humidity

2.1.2 Low Cost Computing Device

Besides sensors and signal conditioning circuitry, the DAQ system requires a computational engine that is able to monitor the sensor outputs and perform the required mathematical transformations to the data and communicate the results with the VOLTRON message bus. Typically, in HVAC applications, a low cost microcontroller is used for data acquisition purposes. Most microcontrollers by themselves do not have the type of communications abilities that are required by the VOLTRON communication protocol. While with enough time and effort, this could be implemented in some microcontrollers, an alternative type of device was selected to perform the required data analysis and communications.

The BeagleBone Black is a low-cost, open-source, community supported development platform with TI Sitara™ ARM® Cortex A8 microprocessor that is capable of running the Linux operating system. In other words, the BeagleBone Black is a computer with all the components (microprocessor, RAM, hard drive, etc.) on a single circuit board. The first role of the BeagleBone Black in this application is to provide analog and digital interfaces between the DAQ software and the required sensors installed on the RTU. Compared to other microcontrollers and microprocessors, application development using the BeagleBone Black is easier since many of these low-level hardware and software interfaces are provided out of the box. The second role of the BeagleBone Black is to support a run-time environment for the central VOLTRON™ application as well as the embedded RTU AFDD software agents. The BeagleBone



Black is not the only system capable of this; other development platforms are available with similar functionality. Development using the BeagleBone Black was selected since the TI Sitara™ microprocessor is widely available. Because of this, any work done with the prototype platform is almost directly translatable to any future platform using a similar chipset.

2.2 Initial Prototype and Testing

Using the sensor requirements described in Tables 2.1-4, electronics system designs were developed that measured all the required state points. The design is shown in Figure A.1 of the Appendix. An initial prototype of the RTU AFDD system was designed and built using electronics hardware and is shown in Figure 2.1. The hardware selected for the prototype is generally considered to be typical and relatively low-cost when compared to similar data acquisition applications within the HVAC market. The prototype was also designed to simplify assembly and debugging so a few components not typically found in an actual application are used, namely the solderless breadboard (which can easily be swapped with a more permanent through-hole perforated board or printed circuit board) and the microprocessor development platform.



Figure 2.1. AFDD breadboard prototype hardware including the BeagleBone Black development platform and thermistor temperature sensors.

After implementing the proof-of-concept prototype using the breadboard system, a through-hole prototype was developed. The through-hole prototype is pictured in Figure 2.2. The system used the same Beaglebone Black single board computer but sensor measurement electronics were soldered onto prefabricated through-hole boards. Due to size constraints, the electronics circuits had to be split between two of the prefabricated prototyping boards.



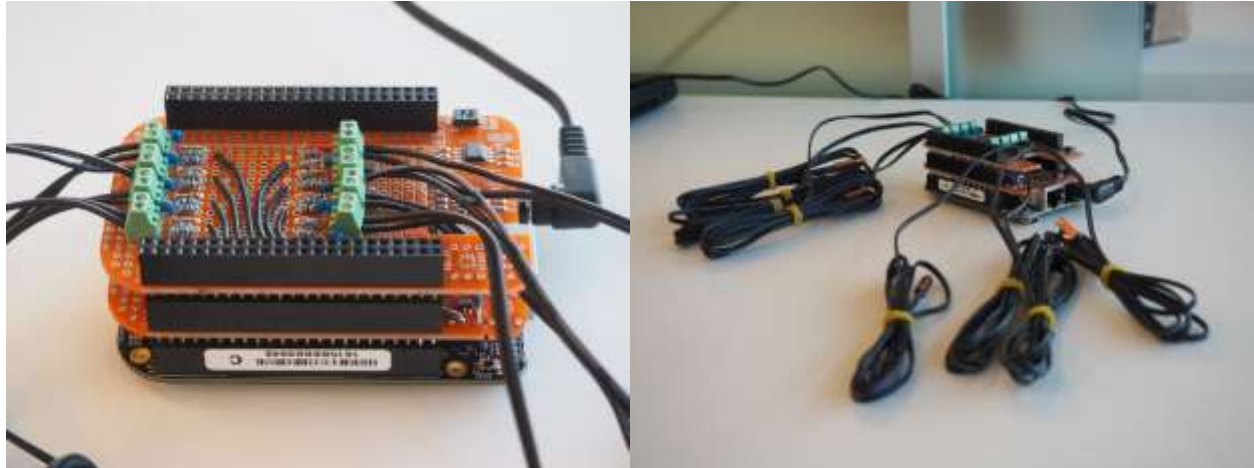


Figure 2.2. RTU AFDD system through-hole prototype implementation using pre-fabricated prototyping electronics boards.

Following the implementation of the through-hole prototype, a printed circuit board design for the RTU AFDD system was developed using electronics CAD software, shown in Figure 2.3. The printed circuit board design could be made much more compact with the use of surface mount components. It can also be mass produced at a much lower costs and with greater reliability when compared with the through hole fabrication process.

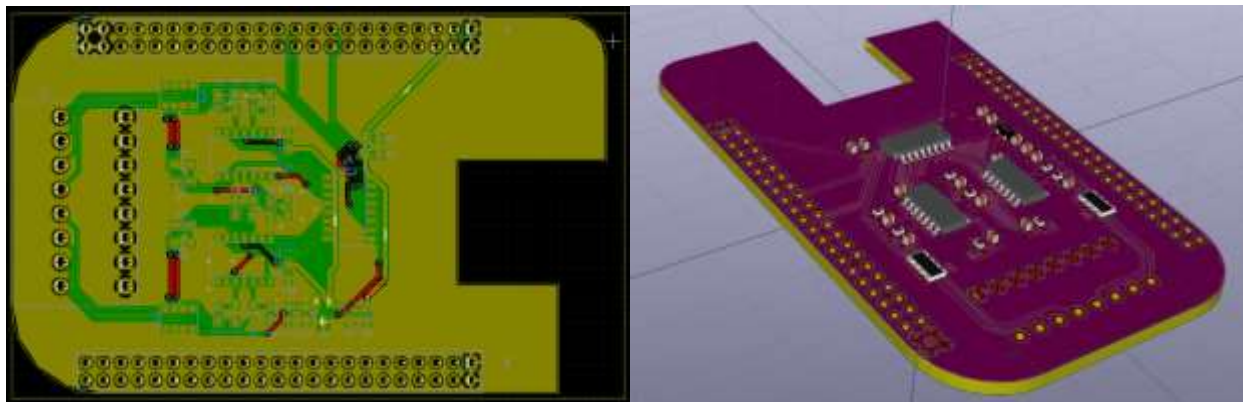


Figure 2.3. Using electronics CAD software, a printed circuit board (PCB) design of the RTU AFDD system was developed.

2.3 Initial Hardware Cost Study

Using costs of the required components from an electronics distributor (Digi-Key Electronics., 2015), the component costs of the designed prototype were determined (found in Table A.2). Subsequently, an estimation of how much the component costs could be reduced by scaling up production was performed using the same distributor's costs at larger quantities. The result of this study is shown in Figure 2.4 for different number of units manufactured.

Figure 2.4 shows that significant component cost reductions (20-25%) can be realized when larger quantities are produced. It can also be seen that an on-board implementation of the virtual evaporator



airflow rate sensor adds a significant cost to the system, approximately \$30 per unit. The study also showed that the BeagleBone Black development platform is not a good component for an actual application since the price remained a constant \$55.00 for all quantities of production. This is expected since the device is intended for prototyping and not for an actual product. To estimate the actual cost of a system, the TI Sitara™ microprocessor used in the BeagleBone Black was priced at different quantities and an additional 20% was added to account for other required components for the low-level interfaces.

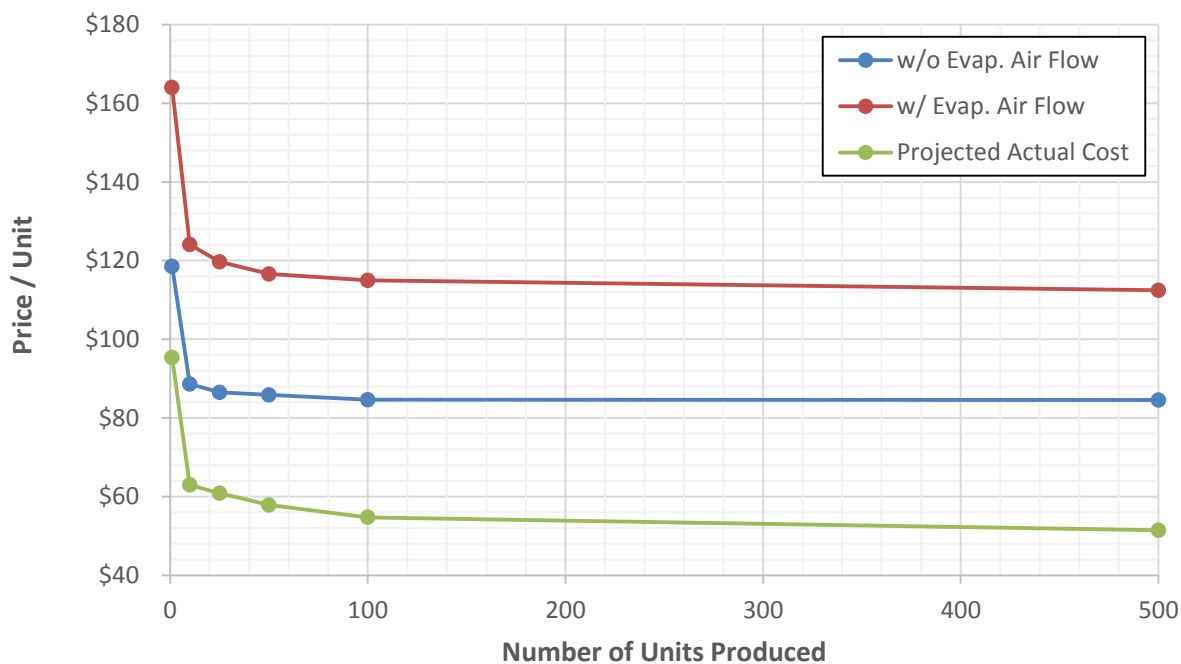


Figure 2.4. Projected RTU AFDD system prototype component costs based on distributors' component cost at different quantities of production.

The initial cost study presented shows that the designed system has promise for future commercial production due to the relatively low component costs. It must also be noted that this study is not complete; only the component costs were detailed. Additional costs to manufacture the systems, as well as engineering and development costs must be accounted for. Nonetheless, this is a positive first step in the development of a commercial ready RTU AFDD system.



3 Description of AFDD Software

The underlying software architecture driving the RTU AFDD system is shown in Figure 1.1 in relation to existing RTU control units. In the proposed system, an agent-based approach relying on the VOLTTRON™ platform is used. The software agents used within the system are segmented: some of the software resides on a dedicated RTU AFDD microprocessor embedded within the equipment while other software potentially resides on a separate server. The software agents embedded into the RTU AFDD microprocessor are the VOLTTRON™ message bus, the data acquisition (DAQ) agent, the virtual sensor agent, and the fault detection and diagnostics agents. On a remote server a database agent, a fault impact evaluation agent, and a service decision-making agent run in response to the outputs from the embedded agents.

The RTU AFDD system software has been implemented using the Python programming language. Python offers several advantages over other programming languages, including development ease and speed, implicit code organization, and many scientific computing packages. All packages used in the RTU AFDD system are open-source and freely available. The VOLTTRON™ platform has also been implemented using Python, which has further eased the RTU AFDD system integration.

The DAQ agent software is used to interface with the installed sensors in order to collect measurements and data for processing. The sensor outputs are polled periodically using digital interfaces provided by the BeagleBone Black device. The thermistor temperature sensors are polled via the serial peripheral interface (SPI) on the BeagleBone Black that is connected to a 12-bit analog-to-digital converter. The air-side temperature and relative humidity sensors are individually addressable via the inter-integrated circuit (I²C) interface on the BeagleBone Black. At a software configurable frequency, the DAQ agent emits time-stamped measurements to the message bus via JSON encoded messages.

Whenever a DAQ agent measurement message is emitted, the virtual sensor agent receives the message via the publish-subscribe (PUB/SUB) pattern implemented in the VOLTTRON™ platform. The virtual sensor agent uses the measurements to evaluate each virtual sensor model used in the RTU AFDD system. Because of this, tuned virtual sensor parameters must be set on initialization using a JSON encoded configuration file. Like the DAQ agent, the virtual sensor agent produces a JSON encoded message containing the virtual sensor model outputs that is emitted to the message bus.

The fault detection and diagnosis agents subscribe to both the DAQ messages and the virtual sensor messages in order to evaluate reference models and determine if the RTU is operating correctly. This is implemented using statistical classifiers that determine the likelihood that the data observed from the current system is different than what is expected. Based on these statistical tests, the status of the equipment is reported via a message sent to the message bus.

The fault evaluation agent consumes all the information produced by previously described agents and determines the impacts the fault have on system performance. Impacts on cooling capacity, COP, run-time, and energy are all determined using measurements of actual performance via the DAQ and virtual



sensor agents and estimations of expected performance. This information is then used to support a service decision-making agent that intends to optimize maintenance costs by calling for service only when needed.

Finally, the last major agent implemented in the RTU AFDD system is one that records all historical data produced by the other agents in the system. This has been implemented in Python using a software connection to a SQLite database. While SQLite would not be the mostly likely database used in a production system, it offers ease of management and can be used to demonstrate the capability of this completed system most easily.

3.1 Data Acquisition Agent Description

The data acquisition (DAQ) agent is used to provide an interface between the sensors installed on the RTU and the VOLTTRON message bus (and by extension, the other AFDD agents connected). This makes it a unique agent in that it is the only agent that directly “interacts” with the RTU system. At a high level, the DAQ agent takes a measurement from each of the sensors at some sampling frequency and publishes these measurements to the VOLTTRON message bus at some publishing frequency. A more detailed overview of this DAQ agent process is shown using a flow chart in Figure 3.1.

Methods have been implemented with the DAQ agent to measure the analog sensor outputs (thermistors used to measure refrigerant-side and condenser air temperatures) and the digital sensor outputs (combined temperature and relative humidity sensors used to measure evaporator air conditions).

3.2 Virtual Sensor Agent Description

Whenever a DAQ agent measurement message is emitted, the virtual sensor agent receives the message via the publish-subscribe (PUB/SUB) pattern implemented in the VOLTTRON™ platform. The virtual sensor agent uses the measurements to evaluate each virtual sensor model used in the RTU AFDD system. Because of this, tuned virtual sensor parameters must be set on initialization using a JSON encoded configuration file. Like the DAQ agent, the virtual sensor agent produces a JSON encoded message containing the virtual sensor model outputs that is emitted to the message bus.

Two main processes are evaluated when a DAQ message is received. First, thermodynamic properties of each RTU system state point are determined. This includes determining saturation temperatures or saturation pressures and the enthalpy of different refrigerant-side and air-side state points. A more detail description of this process is described in Section 3.2.1. After the required thermodynamic properties have been determined, each virtual sensor output is determined. This includes evaluating semi-empirical sensors like the VRC sensor and physics based sensors like the condenser or evaporator airflow sensors. The virtual sensors implemented in the virtual sensor agent are described in Section 3.2.2.



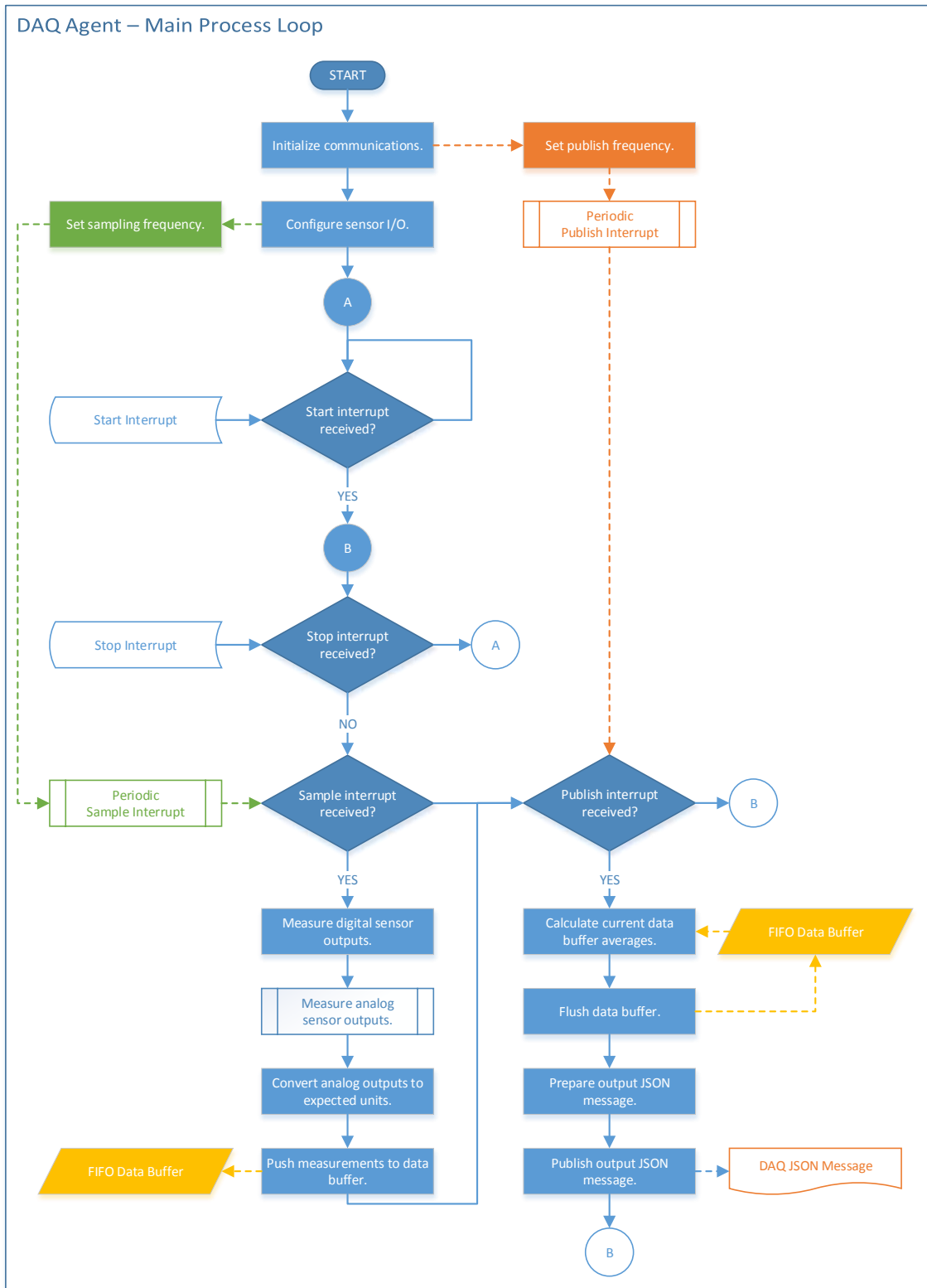


Figure 3.1. Flow chart depicting the main procedure used by the DAQ agent to measure sensors used by the RTU AFDD algorithms and to publish the results to the message bus.



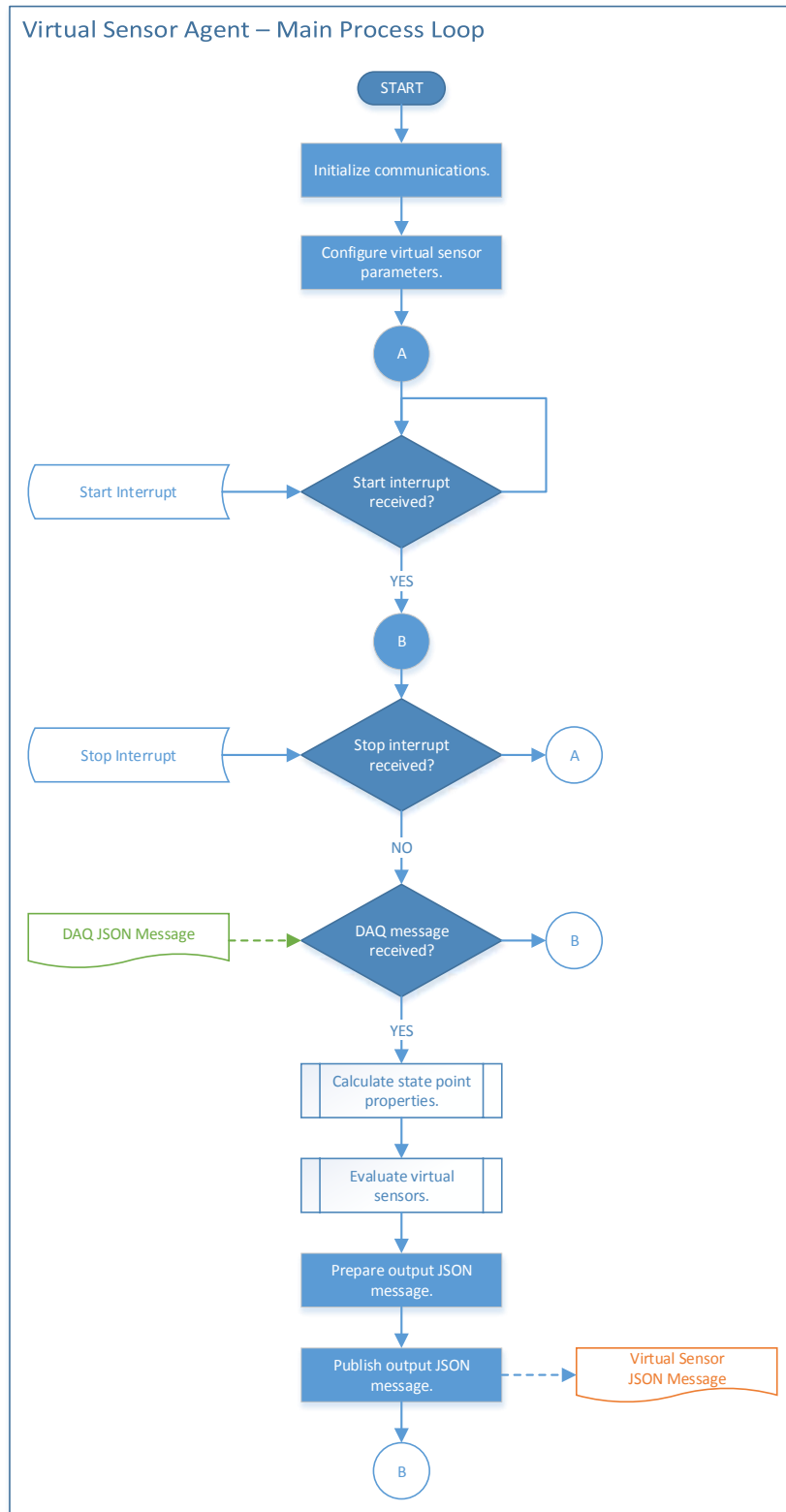


Figure 3.2. Flow chart depicting the main procedure used by the virtual sensor agent to evaluate virtual sensor models using DAQ agent outputs. The agent publishes the results to the message bus.



3.2.1 Thermodynamic Property Calculation Details

The virtual sensors implemented by the virtual sensor agent take advantage of thermodynamic property relations in order to estimate refrigerant and humid air properties at a given state. For refrigerants, fluid properties such as enthalpy, density, etc., can be calculated when two independent state properties are known for a given state. In cases when a refrigerant is not a two-phase mixture (either superheat vapor or subcooled liquid), the refrigerant temperature and pressure are enough to calculate any other property. For humid air calculations, three independent properties are required to fix the state point. An assumption is made by the virtual sensor agent implementation that the atmospheric pressure remains constant so that only a dry-bulb measurement and a relative humidity measurement is required.

Figure 3.3 shows a data flow diagram showing how direct system measurements are used to calculate the enthalpy of the different state points around the system. In Figure 3.3, it is assumed that no system pressures are measured and must be calculated using evaporating and condensing temperatures. The saturation pressure, $P_{r,sat}$, of a two-phase refrigerant can be calculated as a function of its saturation temperature, $T_{r,sat}$,

$$P_{r,sat} = P(T_{r,sat}) \quad (3.1)$$

where P is a function determined from a thermodynamic equation of state used to relate saturation pressure to saturation temperature of the refrigerant. When system pressures are measured, the inverse of Equation (3.1) can be used to calculate the saturation temperature from saturation pressure.



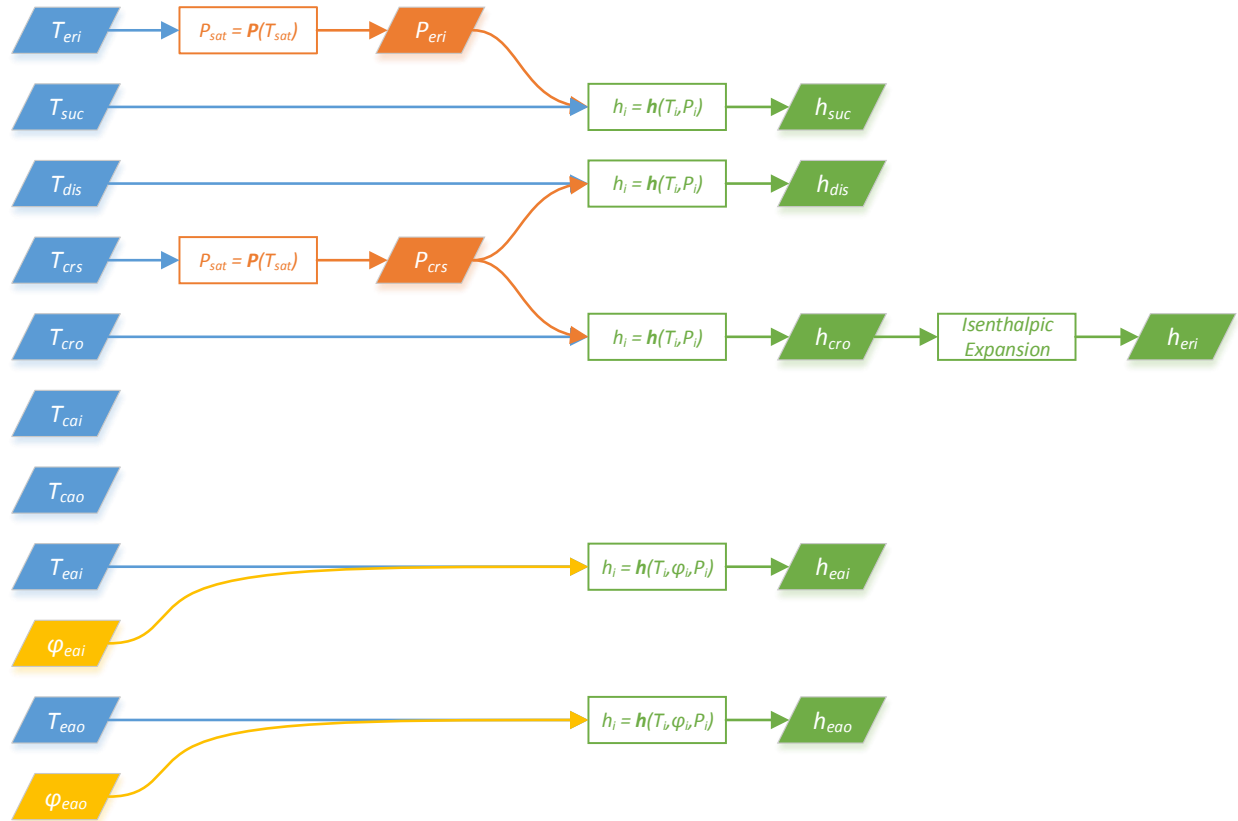


Figure 3.3. Data flow diagram showing how measured sensor outputs are used to determine other fluid properties using thermodynamic equation of state calculations.

In order to measure the saturation temperature, past researchers have used surface-mounted temperature sensors on the evaporator and condenser coil. Measuring the evaporator saturation temperature is straightforward since the entering refrigerant is always inside the two-phase dome. Thus, a sensor mounted near the inlet of the evaporator coil closely approximates the evaporator saturation temperature. Measuring the condenser saturation temperature is less straight-forward since a portion of the coil is used for desuperheating and another portion is used for subcooling the refrigerant. For a finned-tube condenser coil, a surface mounted temperature sensor on one of the return bends of the condenser coil circuits can be used to measure the condenser saturation temperature. Some trial and error may be required to ensure the refrigerant flowing through the return bend chosen is in the two-phase regime.

One further simplification is a negligible pressure drop assumption along the low- and high-sides of the system. That is, the compressor discharge pressure, $P_{r,dis}$, is the same as the condenser saturation pressure, $P_{cr,sat}$, and is the same as the condenser outlet pressure, P_{cro} ,

$$P_{r,dis} = P_{cr,sat} = P_{cro} \quad (3.2)$$

and

$$P_{eri} = P_{er,sat} = P_{r,suc} \quad (3.3)$$



where P_{eri} is the evaporator refrigerant inlet pressure, $P_{er,sat}$ is the evaporator refrigerant saturation temperature, $P_{r,suc}$ and is the compressor refrigerant suction pressure. This simplification significantly reduces the instrumentation costs since no pressure transducers are required for property evaluation when it is possible to measure the saturation temperature. Additionally, the simplification can be justified by the relatively low pressure drops experienced in packaged air conditioners.

For correctness, it should also be noted that Equation (3.1) is only technically valid for pure fluids. In order to determine the saturation pressure of a multi-component mixture, e.g. R410A or R407C, and additional state parameter must be present, most typically the vapor quality or enthalpy. Since these quantities are not generally measurable, this could pose a problem if the pressure glide of the refrigerant is significant. However, for most refrigerants used in packaged systems, this is not the case and Equation (3.1) can be applied with reasonable accuracy.

3.2.2 Virtual Sensor Evaluation Details

Virtual Refrigerant Charge (VRC) Sensor

The purpose of the virtual refrigerant charge sensor is to estimate the current refrigerant charging level of an RTU in order to perform fault detection and diagnosis. The methodology requires four sensors used to measure the compressor suction superheat and the condenser outlet subcooling. The superheat and subcooling of the refrigeration cycle are highly sensitive to the amount of charge in the system. Compressor suction superheat, ΔT_{sh} , is measured using a measurement of the evaporator refrigerant inlet temperature (also evaporator saturation temperature), T_{eri} , and the compressor refrigerant suction temperature, T_{suc} :

$$\Delta T_{sh} = T_{suc} - T_{eri}. \quad (3.4)$$

The evaporator saturation temperature can be measured using a surface-mounted temperature sensor at the evaporator inlet or using a pressure transducer at the compressor suction using thermodynamic property relations.

Similarly, the condenser outlet subcooling, ΔT_{sc} , can be measured using a measurement of the condenser refrigerant saturation temperature, T_{crs} , and the condenser refrigerant outlet temperature, T_{cro} :

$$\Delta T_{sc} = T_{crs} - T_{cro}. \quad (3.5)$$

The condenser saturation temperature can be measured using a surface-mounted temperature sensor on a carefully chosen condenser coil return bend or using a pressure transducer at the compressor discharge using thermodynamic property relations.

The virtual refrigerant charge sensor estimates the relative amount of refrigerant in the system compared to the mass of rated charge, m_{rated} , and takes the following form,



$$\frac{m_{actual} - m_{rated}}{m_{rated}} = 1 + k_{sh}(\Delta T_{sh} - \Delta T_{sh,rated}) + k_{sc}(\Delta T_{sc} - \Delta T_{sc,rated}) + k_x(x_{eri} - x_{eri,rated}) \quad (3.6)$$

where $\Delta T_{sc,rated}$ and $\Delta T_{sh,rated}$ are the subcooling and superheat at the rating condition, respectively, and $x_{eri,rated}$ is the evaporator refrigerant inlet quality at the rating condition. The VRC sensor has three empirically derived coefficients, k_{sh} , k_{sc} , and k_x , that are determined using least-squares regression for a particular RTU using laboratory data.

Virtual Compressor Power (VCP) Sensor

The virtual compressor power sensors are used to estimate the compressor power for fault detection and diagnosis and to estimate the performance impact of different faults. This virtual sensor is essentially a performance mapping of the compressor power under different operating conditions. This requires two temperature sensors to evaluate the VCP sensor: the evaporator saturation temperature, T_{ers} , and condenser saturation temperature, T_{crs} . The form of the compressor power sensor is applicable for constant speed compressors:

$$VCP_I = a_0 + a_1 T_{ers} + a_2 T_{crs} + a_3 T_{ers}^2 + a_4 T_{ers} T_{crs} + a_5 T_{crs}^2 + a_6 T_{ers}^3 + a_7 T_{ers}^2 T_{crs} + a_8 T_{ers} T_{crs}^2 + a_9 T_{crs}^3 \quad (3.7)$$

where $a_{0...9}$ are empirical coefficients that can be obtained from a manufacturer's data sheet. When a compressor with multiple stages is used on the system, a set of empirical coefficients are required for each stage.

Virtual Refrigerant Mass Flow Rate (VRMF) Sensor I

The virtual refrigerant mass flow rate sensor is used to estimate the refrigerant mass flow rate for fault detection and diagnosis. The first virtual mass flow sensor is essentially a map of the compressor under different operating conditions like the VCP sensor. When the compressor is operating properly (free of compressor valve leakage faults) the mapped mass flow rate and actual mass flow rate should agree. The VRMF performance mapping requires two temperature sensors: the evaporator saturation temperature, T_{ers} , and the condenser saturation temperature, T_{crs} . The mass flow rate performance map for constant speed compressors is given by

$$VRMF_{map} = a_0 + a_1 T_{ers} + a_2 T_{crs} + a_3 T_{ers}^2 + a_4 T_{ers} T_{crs} + a_5 T_{crs}^2 + a_6 T_{ers}^3 + a_7 T_{ers}^2 T_{crs} + a_8 T_{ers} T_{crs}^2 + a_9 T_{crs}^3 \quad (3.8)$$

where $a_{0...9}$ are empirically determined coefficients. An additional adjustment must be made to the performance map output to account for difference between the actual suction superheat and the superheat maintained during the ratings process. This correlation is given by Dabiri and Rice (1981) and takes the form:

$$VRMF_I = \left[1 + F \left(\frac{\rho_{rated}}{\rho_{actual}} - 1 \right) \right] VRMF_{map} \quad (3.9)$$

where ρ_{actual} and ρ_{rated} are measurements of the actual and rated suction density and F is an empirical parameter usually set to 0.75. In order to determine the actual suction density, system measurements are used by applying the thermodynamic property relations. To determine the rated



suction density, the superheat maintained during the ratings process must be known along with the current evaporating temperature.

Mass Flow Rate (VRMF) Sensor II

The second virtual refrigerant mass flow sensor is used to estimate the refrigerant mass flow rate using an energy balance on the compressor. This virtual sensor should be accurate during normal and faulty operation since it is based on thermodynamic laws. The sensor uses then suction and discharge enthalpy of the compressor along with the output of the VCP sensor:

$$VRMF_{II} = \frac{VCP(1 - \alpha_{loss})}{h_{dis} - h_{suc}} \quad (3.10)$$

where h_{suc} and h_{dis} are the suction and discharge enthalpies and α_{loss} is a heat loss parameter that must be determined using empirical data (though should be small).

Virtual Condenser Airflow (VCAF) Sensor

Condenser fouling is detected and diagnosed with a virtual condenser airflow (VCAF) sensor. The sensor is derived from an energy balance on the condenser of the RTU and uses the enthalpy of the entering and leaving air as well as the inlet and outlet refrigerant enthalpy along with the virtual refrigerant mass flow rate:

$$VCAF = \frac{VRMF_{II}(h_{dis} - h_{cro})}{T_{cao} - T_{cai}} \frac{v_{ca}}{c_{p,ca}} \quad (3.11)$$

where v_{ca} and $c_{p,ca}$ are the specific volume and specific heat of the condenser air respectively. Because the condenser heat rejection process is always dry, the enthalpy change of the condenser air can be calculated using the specific heat of the condenser air and the temperature change.

Virtual Evaporator Airflow (VEAF) Sensor

Evaporator fouling is detected and diagnosed with a virtual evaporator airflow sensor based on an evaporator energy balance. This requires knowledge of the enthalpy entering and leaving air as well as the inlet and outlet refrigerant enthalpy:

$$VEAF = \frac{VRMF_{II}(h_{suc} - h_{eri})}{h_{eai} - h_{cao}} v_{ea} \quad (3.12)$$

where h_{eai} is the evaporator refrigerant inlet enthalpy determined by assuming an isenthalpic expansion process and v_{ea} is the specific volume of the evaporator air. Since moisture removal can be significant across the evaporator, humidity measurements of the entering and leaving evaporator air must be measured in order to determine the enthalpy of the entering and leaving air.

Virtual Cooling Capacity Sensor

One impact that many faults have on an air-conditioning system is a reduction in total cooling capacity. Because of this, the system must run longer to meet a given load and could lead to the system not having enough capacity to maintain comfort conditions during times of high loads. The cooling capacity of a packaged air conditioner can be calculated using Equation (3.13)



$$\dot{Q}_{cool,virtual} = VRMF_{II}(h_{suc} - h_{eri}) \quad (3.13)$$

where $VRMF_{II}$ is the mass flow rate of refrigerant through the evaporator coil, h_{suc} is the refrigerant enthalpy at the evaporator outlet (or compressor suction port), h_{eri} and is the refrigerant enthalpy at the evaporator inlet.

Virtual Coefficient of Performance Sensor

Another important system performance metric is the cycle efficiency or coefficient of performance (COP), given by Equation (3.14).

$$COP_{virtual} = \frac{\dot{Q}_{cool,virtual}}{VCP} \quad (3.14)$$

The total electrical power delivered to the system can be defined in different ways, depending on where system boundaries are defined. Frequently, it is defined as only the electrical power consumed by the compressor. On the other hand, the COP of a system is sometimes calculated by summing the electrical power consumed by the compressor and fans/blowers,

$$\dot{W}_{elec} = \dot{W}_{comp} + \dot{W}_{odf} + \dot{W}_{idf} \quad (3.15)$$

where \dot{W}_{odf} is the outdoor fan power consumption and \dot{W}_{idf} is the indoor fan power consumption. When COP is determined using the sum of compressor and fan powers, a widely used convention is to call this efficiency the coefficient of system performance (COSP).

3.3 Fault Evaluation Agent Description

3.3.1 Virtual-Sensor-Based Fault Impact Ratios

In order to assess the impact of a fault on system performance it is convenient to compare the actual performance of a system with the performance of a normal system at the same operating conditions. One method of comparing the actual and normal performance is to form a fault impact ratio,

$$\text{Fault Impact Ratio} = \frac{\text{Actual Performance}}{\text{Normal Performance}} \quad (3.16)$$

where the numerator of Equation (3.16) is some measure of the actual performance of a system and the denominator is the performance of a normal system. In other words, the fault impact ratio defined in Equation (3.16) is an indicator of how much performance has changed relative to the performance that is normally expected. Several indicators of performance can be directly represented by these fault impact ratios, including cooling capacity, cycle efficiency, sensible capacity, and ventilation load.

Cooling Capacity Impact Ratio

One of the most important results of several common faults commonly affecting packaged air conditioners is a reduction in total cooling capacity. This impact can be quantified by substituting cooling capacity into Equation (3.16), yielding

$$r_{cool} = \frac{\dot{Q}_{cool,actual}}{\dot{Q}_{cool,normal}} \quad (3.17)$$



where $\dot{Q}_{cool,actual}$ is the actual cooling capacity of the system and $\dot{Q}_{cool,normal}$ is the normal cooling capacity of the system without faults. When faults are present in the system that degrade cooling capacity, such as low refrigerant charge or a fouled evaporator coil, r_{cool} becomes less than 1; in the case where a fault positively affects a system's cooling capacity, an overcharged system with a fixed orifice for example, r_{cool} becomes greater than 1. In the trivial case when the system is normal, $r_{cool} = 1$.

In order to evaluate Equation (3.17), a measurement of the actual cooling capacity, $\dot{Q}_{cool,actual}$, and an estimate of the normal cooling capacity, $\dot{Q}_{cool,normal}$, are required. A measurement of the actual cooling capacity is achieved with the same virtual cooling capacity sensor used in the virtual sensor agent, defined in Equation (3.13). The normal cooling capacity is estimated using performance reference models that equipment manufacturers may have or using performance map data.

Sensible Cooling Capacity Impact Ratio

The total cooling capacity that an air conditioning system delivers is made up of a sensible component and a latent component. The sensible component of the total capacity is especially important for packaged air conditioners since they are generally controlled based only on the dry-bulb temperature of the conditioned space. Thus, a reduction in sensible cooling capacity may have a greater impact than a reduction in latent cooling capacity.

To characterize the sensible cooling capacity impact of a fault on a system, it is useful to use the sensible heat ratio,

$$SHR = \frac{\dot{Q}_{cool,sensible}}{\dot{Q}_{cool,total}} \quad (3.18)$$

where $\dot{Q}_{cool,sensible}$ is the sensible cooling capacity and $\dot{Q}_{cool,total}$ is the total cooling capacity delivered. Using Equations (3.16) and (3.18), the sensible capacity impact can be defined

$$r_{SHR} = \frac{SHR_{actual}}{SHR_{normal}} \quad (3.19)$$

where using the same convention as before SHR_{actual} is the actual sensible heat ratio and SHR_{normal} is the normal sensible heat ratio delivered by the system. Evaluation of Equation (3.20) requires air-side measurements since it is not possible to measure the sensible capacity from refrigerant measurements alone.

Coefficient of Performance Impact Ratio

The change in COP caused by a fault can be measured using an impact ratio,

$$r_{COP} = \frac{COP_{actual}}{COP_{normal}} \quad (3.20)$$

where COP_{actual} is the actual efficiency of the system determined using the virtual COP sensor and COP_{normal} is the normal efficiency a fault free system is expected to have at the same conditions. The



COP impact ratio provides an indication of 1.) a change in total capacity of the system and 2.) a change in the electrical power consumption of the system.

Run-Time Impact Ratio

With reduced cooling capacity or increased ventilation load, one effect that faults have on an air-conditioning system is increased in run-time. Longer run-time has at least two effects: 1.) increased energy usage and 2.) decreased equipment life (with the assumption that a typical air conditioner operates for a finite number of hours). A packaged air conditioner is typically operated by a thermostat controlling the dry bulb temperature of a conditioned space to some set point. Thus, the run-time of the air conditioner is related to the total cooling load and cooling capacity delivered,

$$\Delta t_{run} = \frac{Q_{load}}{\dot{Q}_{cool}} \quad (3.21)$$

where Q_{load} is the total cooling load of the conditioned space and \dot{Q}_{cool} is the total cooling capacity. If it is assumed the thermostat maintains the sensible load of the space, the run-time can be related to the sensible cooling capacity instead,

$$\Delta t_{run} = \frac{Q_{load}}{SHR \cdot \dot{Q}_{cool}} \quad (3.22)$$

where SHR is the sensible heat ratio. Using Equation (3.22), a run-time impact ratio is defined,

$$r_{run} = \frac{\Delta t_{run,actual}}{\Delta t_{run,normal}} \quad (3.23)$$

where $\Delta t_{run,actual}$ is the actual run-time required by the air conditioning system and $\Delta t_{run,normal}$ is the run-time requirement for a normal system without faults. Combining Equations (3.22) and (3.23) yields an expression for the run-time impact ratio in terms of three other impact ratios,

$$r_{run} = \frac{r_{load}}{r_{SHR} r_{cool}} \quad (3.24)$$

where r_{load} is relative increase in the cooling load caused by faults, r_{SHR} is the sensible heat impact ratio, r_{cool} and is the cooling capacity impact ratio. Equation (3.24) shows that the run-time impact increases as the cooling load impact increases and increases as the sensible heat ratio or cooling capacity impacts decrease.

The cooling load impact ratio, r_{load} , presents a possible problem for estimating the run-time impact of different faults. This is because the load of the conditioned space is unknown to the air conditioner and measuring it is unfeasible. These problems can be overcome by assuming that any fault affecting the refrigeration cycle (improper charge, fouling, etc.) has no impact on the load of the conditioned space. In other words, the impact of a fault on the conditioned space load is $r_{load} = 1$.

Energy Impact Ratio

The electrical energy usage of an air conditioner can be calculated over some given run-time, Δt_{run} , using Equation (3.25)



$$W_{elec} = \frac{\dot{Q}_{cool}}{COP} \Delta t_{run} \quad (3.25)$$

using the cooling capacity, \dot{Q}_{cool} , and the coefficient of performance, COP, of the system. The performance impact ratio for electrical energy usage can be determined using Equation (3.26),

$$r_W = \frac{W_{elec,actual}}{W_{elec,normal}} \quad (3.26)$$

using the same conventions for actual and normal energy usage. When Equations (3.25) and (3.26) are combined, the energy impact ratio can be expressed as

$$r_W = \frac{r_{cool}}{r_{COP}} r_{run} \quad (3.27)$$

using Equations (3.17), (3.20), and (3.24) for r_{cool} , r_{COP} , r_{run} and respectively.

1.2. Fault Detection and Diagnosis Methodology

Using virtual sensors, faults are identified and classified by the FDD system using statistical methods. In the general case, it is expected an indicator of faulty operation can be observed using the virtual sensors. To determine if a fault exists, the virtual sensor output is compared to the output of a model for expected performance. In the case of determining if a system is properly charged, this could simply be comparing the VRC sensor output to the rated charge level. By sampling data, two empirical distributions are generated over time: one for the observed behavior and one for the expected behavior. While these data could be sampled from many types of random distributions, it is assumed in the FDD system that both cases are sampled from normal distributions with measurable means and standard deviations. Figure 3.4 shows a diagram of a case where the observed distribution appears to be different from the expected distribution.



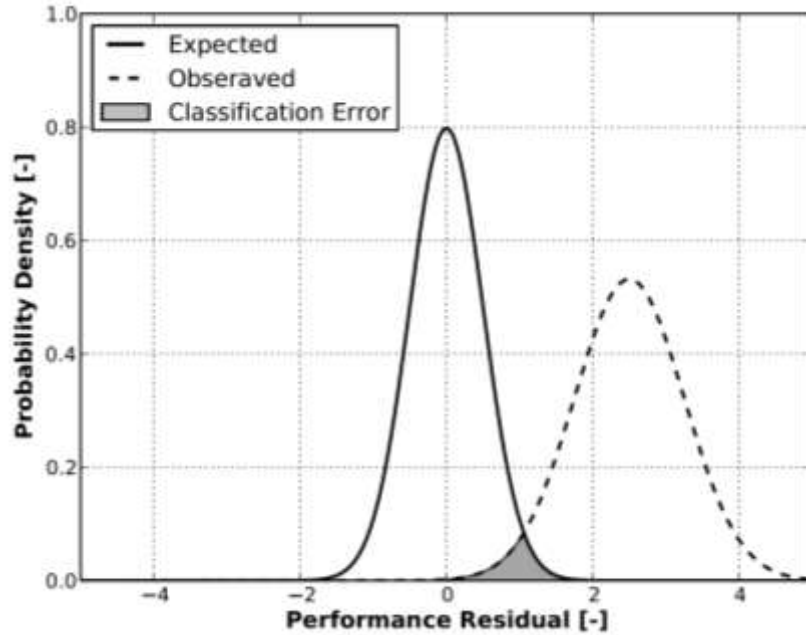


Figure 3.4. The probability that a fault is present is determined by calculating the probability that the observed data and the expected data are derived from the same distribution. This probability is calculated by integrating the area of overlap between the two probability density functions.

The probability that a fault is present is determined by calculating the probability that the observed data and the expected data are derived from the same distribution. This probability is calculated by integrating the area of overlap between the two probability density functions (pdf). Noting that the probability density function of a normal random variable is given by

$$f(x|\mu, \sigma) = \frac{1}{\sigma\sqrt{2\pi}} \exp\left[-\frac{(x - \mu)^2}{2\sigma^2}\right] \quad (3.28)$$

then the intersection, b , of two normal distributions can be calculated by equating the pdfs of the observed and expected samples:

$$f_{obs}(b|\mu_{obs}, \sigma_{obs}) = f_{exp}(b|\mu_{exp}, \sigma_{exp})$$

$$\frac{1}{\sigma_{obs}\sqrt{2\pi}} \exp\left[-\frac{(b - \mu_{obs})^2}{2\sigma_{obs}^2}\right] = \frac{1}{\sigma_{exp}\sqrt{2\pi}} \exp\left[-\frac{(b - \mu_{exp})^2}{2\sigma_{exp}^2}\right]$$

$$b = \frac{\mu_{obs}\sigma_{exp}^2 - \sigma_{exp} \left(\mu_{obs}\sigma_{exp} \pm \sigma_{obs} \sqrt{(\mu_{obs} - \mu_{exp})^2 + 2(\sigma_{obs}^2 - \sigma_{exp}^2) \log\left(\frac{\sigma_{obs}}{\sigma_{exp}}\right)} \right)}{\sigma_{obs}^2 - \sigma_{exp}^2} \quad (3.29)$$

To calculate the probability that the two sample distributions are the same, the cumulative density function of a normal distribution is used

$$F(x|\mu, \sigma) = \frac{1}{2} \left[1 + \operatorname{erf}\left(\frac{x - \mu}{\sigma\sqrt{2}}\right) \right] \quad (3.30)$$

by calculating the probability enclosed by the two distributions:



$$\begin{aligned}
P(C_{obs} = C_{obs} | \mu_{obs}, \mu_{exp}, \sigma_{obs}, \sigma_{obs}) &= P(C_{exp} > b) + P(C_{obs} < b) \\
&= 1 - F_{exp}(b | \mu_{exp}, \sigma_{exp}) + F_{obs}(b | \mu_{obs}, \sigma_{obs}) \\
&= 1 - \frac{1}{2} \operatorname{erf}\left(\frac{b - \mu_{exp}}{\sigma_{exp}\sqrt{2}}\right) + \frac{1}{2} \operatorname{erf}\left(\frac{b - \mu_{obs}}{\sigma_{obs}\sqrt{2}}\right)
\end{aligned} \tag{3.31}$$

In order to determine the probability that the fault is present, the probability that the observed and expected samples distributions are different must be calculated. This probability is calculated using Equation (3.31),

$$P(C_{obs} \neq C_{obs} | \mu_{obs}, \mu_{exp}, \sigma_{obs}, \sigma_{obs}) = 1 - P(C_{obs} = C_{obs} | \mu_{obs}, \mu_{exp}, \sigma_{obs}, \sigma_{obs}) \tag{3.32}$$

This procedure is used to calculate the probabilities that the system is not charged to the correct level, if there is a reduction in evaporator airflow (indicating evaporator fouling), or if there is a reduction in condenser airflow (indicating condenser fouling). Additionally, degradations in total cooling capacity or COP can be calculated using this procedure.



4 VOLTRON RTU AFDD System Test Results

In an effort to assess the effectiveness of the FDD system applied to different types of RTUs, extensive testing within psychrometric chambers has been performed. Testing and evaluation of the FDD system has been carried out for four systems termed System A, B, C, and D.

System A: RTU with Microchannel Condenser and Thermostatic Expansion Device

The first system tested in the psychrometric chamber test facilities was System A (microchannel condenser, thermostatic expansion valve). The empirical parameters of the VRC model were determined using the automated open laboratory training algorithm (described in Milestone Report 2.5C). The RTU was installed in the psychrometric chamber test facilities and was tested for both stages of cooling. These test conditions are described in Table 4.1 for low stage and Table 4.2 for high stage.

Table 4.1. Test conditions for RTU with microchannel condenser and thermostatic expansion valve (System A) for low stage cooling operation in psychrometric test chambers.

Test Variable		Test Values
Compressor Stage	[-]	LOW
Indoor Dry Bulb	[°F]	80
Indoor Wet Bulb	[°F]	67
Outdoor Dry Bulb	[°F]	69, 82, 95
Charge Level ¹	[%]	60, 70, 80, 90, 100, 110, 120
Indoor Fan Torque ²	[%]	40, 60
Outdoor Fan Torque ³	[%]	40, 70

¹ Charge is measured relative to the recommended charge according to the manufacturer's nameplate data.

² Indoor fan torque is set according to a nominal flow rate of 1350 CFM for low stage operation.

³ Outdoor fan torque is set using the manufacturer's default value for low stage operation.

Table 4.2. Test conditions for RTU with microchannel condenser and thermostatic expansion valve (System A) for high stage cooling operation in psychrometric test chambers.

Test Variable		Test Values
Compressor Stage	[-]	HIGH
Indoor Dry Bulb	[°F]	80
Indoor Wet Bulb	[°F]	67
Outdoor Dry Bulb	[°F]	82, 95, 108
Charge Level ¹	[%]	60, 70, 80, 90, 100, 110, 120
Indoor Fan Torque ²	[%]	60, 90
Outdoor Fan Torque ³	[%]	70, 100

¹ Charge is measured relative to the recommended charge according to the manufacturer's nameplate data.

² Indoor fan torque is set according to a nominal flow rate of 2000 CFM for high stage operation.

³ Outdoor fan torque is set using the manufacturer's default value for high stage operation.

The resulting accuracy of the VRC sensor models trained in the open laboratory space and applied to the psychrometric chamber test data collected over the range of ambient conditions is shown for both cooling stages in Figure 4.1. The results show that the low-stage cooling tests were less accurate than during high-stage cooling operation. This result was observed for the other systems as well. At low charge levels, the performance of the VRC sensor during low-stage operation was worse. It can be seen that even the training data were less accurately predicted at low charge levels. This was not the case for



high stage cooling operation; the accuracy was relatively the same at all charge levels tested. It should be noted that the root-mean-squared error (RMSE) was less than 10% for both stages of operation. This indicates that the predictions from the VRC sensor are accurate enough for the FDD system to detect faults due to improper charge level.

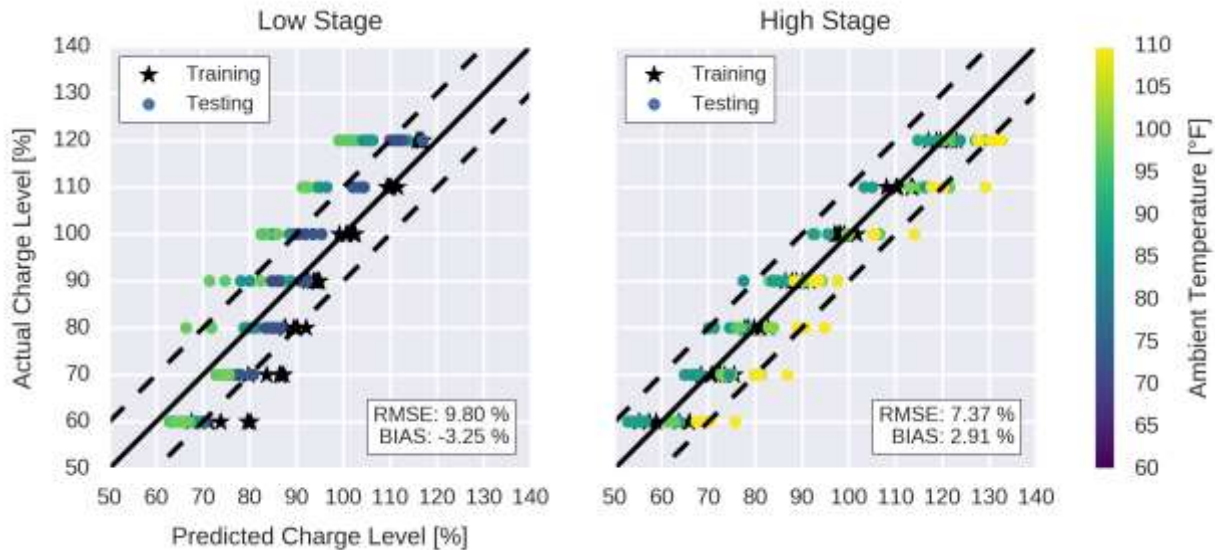


Figure 4.1. VRC sensor prediction accuracy for RTU with microchannel condenser and thermostatic expansion valve (System A) applied to both stages of operation under different ambient conditions.

System B: RTU with Microchannel Condenser and Fixed Orifice Expansion Device

After the completion of testing and evaluating the data collected from System A, the thermostatic expansion valve (TXV) was replaced by a fixed orifice expansion device. The orifice size and design was selected with the help of the original equipment manufacturer to ensure that the performance of the unit was representative of actual units. After the replacement of the expansion device, the RTU was referenced as System B.

The automated open laboratory training kit was applied to System B in an open laboratory space in order to collect data used to determine the empirical parameters of the VRC sensor model. At the conclusion of this process, the RTU was installed in the psychrometric chambers and tested over a range of ambient conditions. The test conditions for low-stage and high-stage operation are described in Table 4.3 and Table 4.4, respectively. These conditions were similar to those tested for System A, but extended to include the high temperature condition during low stage operation and the cool temperature condition during high stage operation.

Table 4.3. Test conditions for RTU with microchannel condenser and fixed orifice expansion device (System B) for low stage cooling operation in psychrometric test chambers.

Test Variable	Test Values
Compressor Stage	[-]
Indoor Dry Bulb	[°F]
Indoor Wet Bulb	[°F]
Outdoor Dry Bulb	[°F]
Charge Level ¹	[%]



Indoor Fan Torque ²	[%]	40, 60
Outdoor Fan Torque ³	[%]	40, 70

¹ Charge is measured relative to the recommended charge according to the manufacturer’s nameplate data.

² Indoor fan torque is set according to a nominal flow rate of 1350 CFM for low stage operation.

³ Outdoor fan torque is set using the manufacturer’s default value for low stage operation.

Table 4.4. Test conditions for RTU with microchannel condenser and fixed orifice expansion device (System B) for high stage cooling operation in psychrometric test chambers.

Test Variable		Test Values
Compressor Stage	[-]	HIGH
Indoor Dry Bulb	[°F]	80
Indoor Wet Bulb	[°F]	67
Outdoor Dry Bulb	[°F]	69, 82, 95, 108
Charge Level ¹	[%]	60, 70, 80, 90, 100, 110, 120
Indoor Fan Torque ²	[%]	60, 90
Outdoor Fan Torque ³	[%]	70, 100

¹ Charge is measured relative to the recommended charge according to the manufacturer’s nameplate data.

² Indoor fan torque is set according to a nominal flow rate of 2000 CFM for high stage operation.

³ Outdoor fan torque is set using the manufacturer’s default value for high stage operation.

The accuracy of the VRC sensor models for System B trained using open laboratory data and applied to the psychrometric chamber test data collected over the range of ambient conditions is shown for both cooling stages in Figure 4.2. The results show that the low-stage cooling tests were less accurate than during high-stage cooling operation. This is especially true when the amount of refrigerant charge contained was above 90%. After analysis of the experimental data, it was determined that for these cases, the system operated with zero superheat or subcooling. One explanation for this is the diameter of the fixed orifice was too large for the low-stage operation. This is understandable since the orifice must be designed for the high stage operation in order to maximize design point performance. Because there was no superheat or subcooling during these data points, the VRC model must rely entirely on the evaporator refrigerant quality term (which is essentially a function of condensing pressure). With this in mind, the performance of the VRC sensor is rather respectable considering the system performance information available. The RMSE error for the low stage operation was on par with the results obtained for System A. The accuracy during high stage operation was actually better than System A at 6.68%.



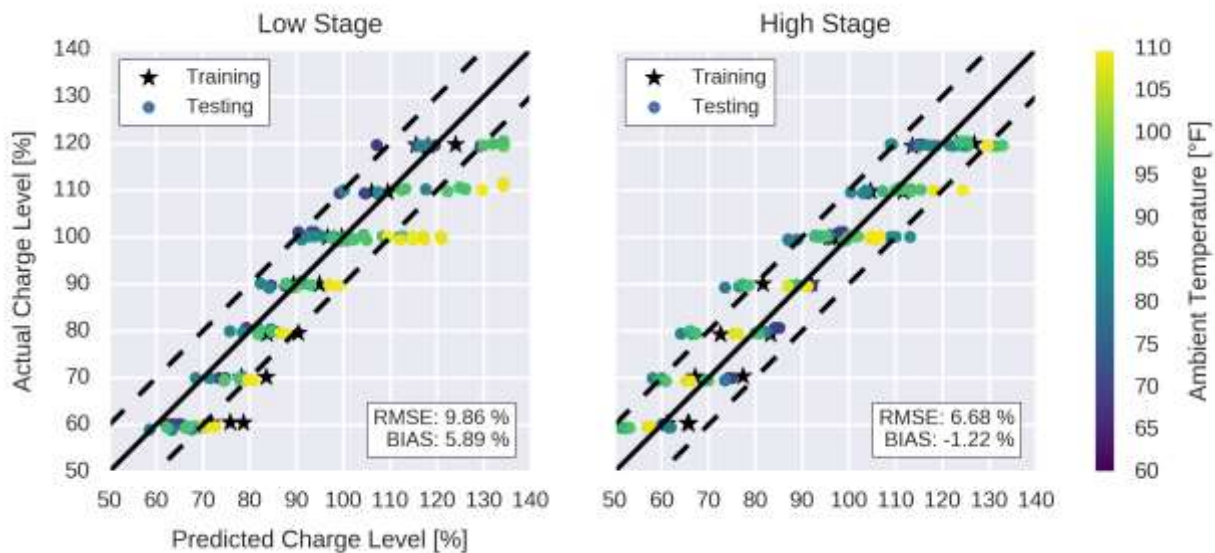


Figure 4.2. VRC sensor prediction accuracy for RTU with microchannel condenser and fixed orifice expansion device (System B) applied to both stages of operation under different ambient conditions.

System C: RTU with Finned Tube Condenser and Fixed Orifice Expansion Device

Following the testing and evaluation of the data collected from System B, the microchannel condenser coil originally installed on the unit was replaced by a finned tube condenser coil. The new coil was received from the original equipment manufacturer. This coil was designed for the RTU and can be ordered as a lower efficiency option. After the replacement of the condenser coil, the RTU was referenced as System C.

Following the System B psychrometric chamber testing, System C was tested in the psychrometric chambers over a wide range of ambient conditions and fault combinations. The conditions tested for low and high stage operation are described in Table 4.4 and Table 4.5, respectively. These test conditions were expanded from System B since the testing was progressing ahead of schedule, including testing at both wet and dry coil conditions for a subset of tests.

Table 4.5. Test conditions for RTU with finned-tube condenser and fixed orifice expansion device (System C) for low stage cooling operation in psychrometric test chambers.

Test Variable	Test Values
Compressor Stage	[-]
Indoor Dry Bulb	[°F]
Indoor Wet Bulb	[°F]
Outdoor Dry Bulb	[°F]
Charge Level ¹	[%]
Indoor Fan Torque ²	[%]
Outdoor Fan Torque ³	[%]

¹ Charge is measured relative to the recommended charge according to the manufacturer’s nameplate data.

² Indoor fan torque is set according to a nominal flow rate of 1350 CFM for low stage operation.

³ Outdoor fan torque is set using the manufacturer’s default value for low stage operation.



Table 4.6. Test conditions for RTU with finned-tube condenser and fixed orifice expansion device (System C) for high stage cooling operation in psychrometric test chambers.

Test Variable		Test Values
Compressor Stage	[-]	HIGH
Indoor Dry Bulb	[°F]	80
Indoor Wet Bulb	[°F]	57, 67
Outdoor Dry Bulb	[°F]	69, 82, 95, 108
Charge Level ¹	[%]	60, 70, 80, 90, 100, 110, 120
Indoor Fan Torque ²	[%]	50, 90
Outdoor Fan Torque ³	[%]	70, 100

¹ Charge is measured relative to the recommended charge according to the manufacturer’s nameplate data.

² Indoor fan torque is set according to a nominal flow rate of 2000 CFM for high stage operation.

³ Outdoor fan torque is set using the manufacturer’s default value for high stage operation.

The accuracy of the VRC model designed for System C for each stage of operation is shown in Figure 4.3 over the range of ambient conditions tested. The performance of the VRC sensor applied to System C was better than System A or System B, which may indicate that a system having a finned tube condenser may be modelled more easily. In both stages of operation, the RMSE was approximately 6.20%. Additionally, the accuracy observed over the range of charge levels was relatively constant.

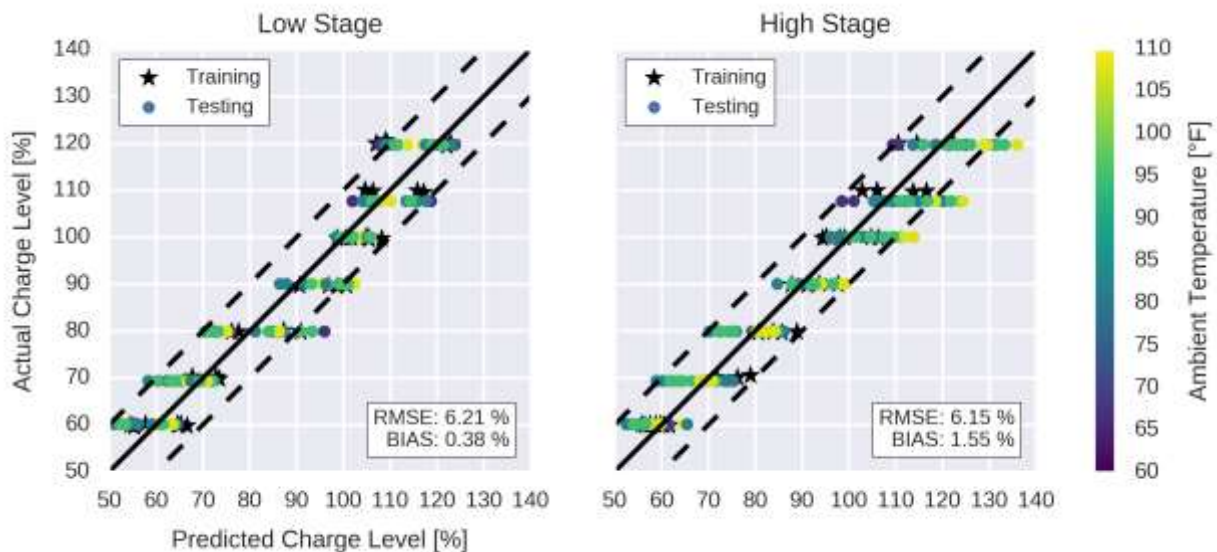


Figure 4.3. VRC sensor prediction accuracy for RTU with finned tube condenser and fixed orifice expansion device (System C) applied to both stages of operation under different ambient conditions.

The accuracy of the VRC sensor applied to System C for cases where refrigerant charge faults were injected into the system is shown in Figure 4.4. Also shown in Figure 4.4 is the calculated probability of a charge fault being present in each case. To calculate this percentage Equation (3.32) was used, assuming that the expected refrigerant charge level is 100% with a standard deviation based on the RMSE determined in Figure 4.3. The results shown in Figure 4.4 show that FDD system is able to identify refrigerant charge faults with probabilities greater than 95% when the actual charge level deviates $\pm 15\%$ from normal.



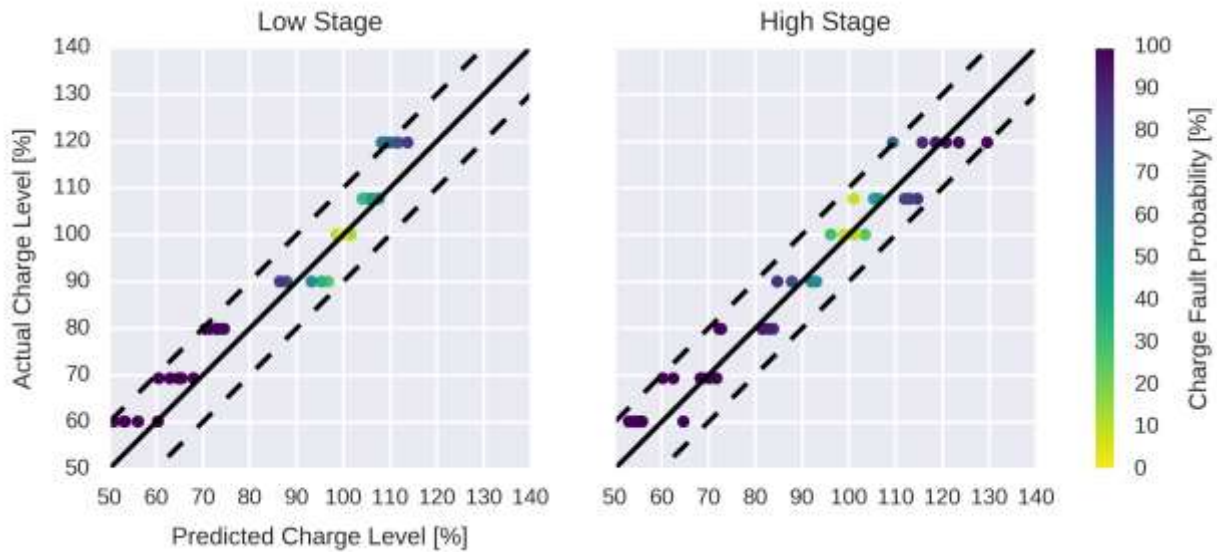


Figure 4.4. Prediction accuracy of VRC sensor applied to charge level vaults only showing charge fault probability for each test case (System C). The data show that the FDD system is able to identify faults with high confidence when actual charge is $\pm 20\%$ of the normal charge level.

It is important that the FDD system is able to accurately identify faults when there are multiple simultaneous faults affecting the system. Figure 4.5 shows the performance of the charge fault diagnostics for several combinations of improper refrigerant levels, indoor airflow levels, and outdoor airflow levels. In these results, tested under 82 °F outdoor temperature, refrigerant charge faults were correctly identified with probabilities greater than 95% in all cases where the charge level deviated by at least $\pm 20\%$. It is also noteworthy that the VRC sensor tends to predict refrigerant charge faults with greater probability when the impact on system capacity of the faults increase. This indicates that when significant refrigerant charge faults affect the system, the FDD system is able to identify them.



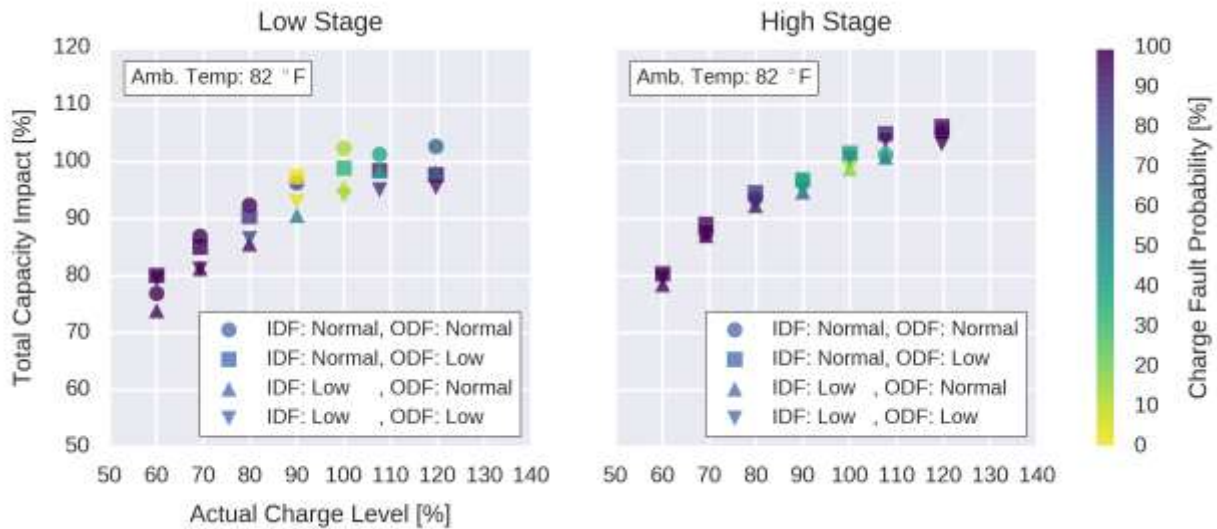


Figure 4.5. Total capacity impact of refrigerant charge faults at 82 °F outdoor ambient temperature (System C). The points are colored based on the fault probability determined for each test case, indicating faults that have larger impacts are identified with greater probability.

Similar results for test conditions at 95 °F and 108 °F outdoor temperature are shown in Figure 4.6 and Figure 4.7 respectively. In these results, refrigerant charge faults were correctly identified with high probabilities in test cases where the refrigerant charge deviated by $\pm 10\%$. It should also be noted that refrigerant charge faults tended to have large impacts on the total capacity of the system at the higher outdoor temperatures.

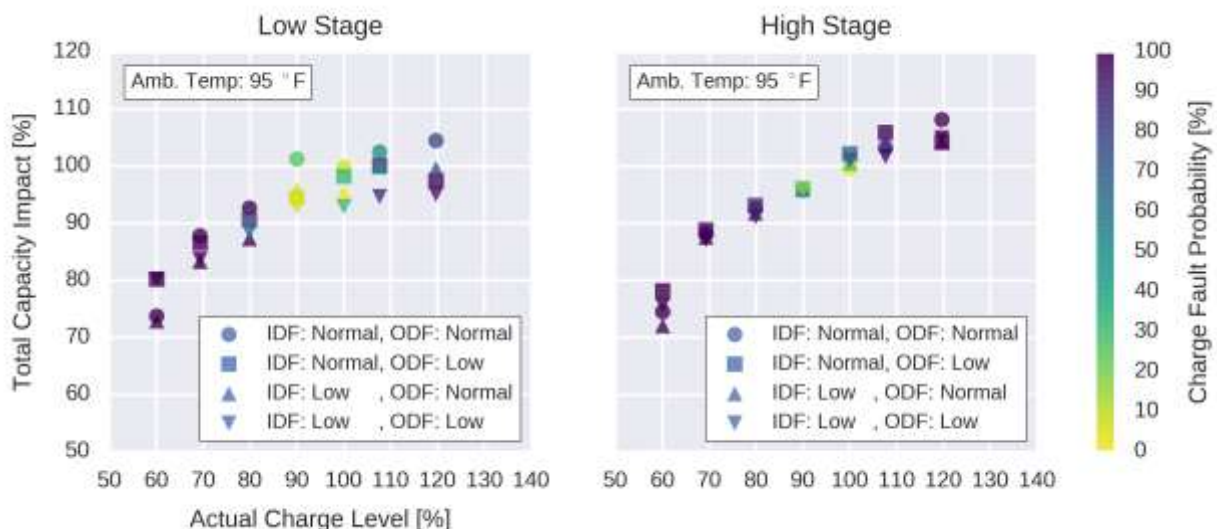


Figure 4.6. Total capacity impact of refrigerant charge faults at 95 °F outdoor ambient temperature (System C). The points are colored based on the fault probability determined for each test case, indicating faults that have larger impacts are identified with greater probability.



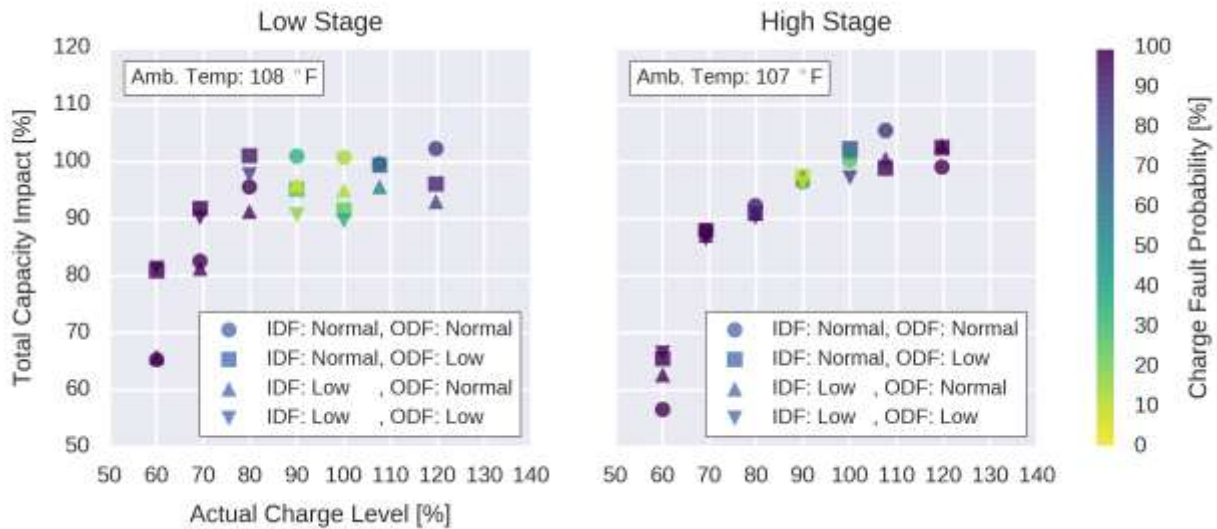


Figure 4.7. Total capacity impact of refrigerant charge faults at 108 °F outdoor ambient temperature (System C). The points are colored based on the fault probability determined for each test case, indicating faults that have larger impacts are identified with greater probability.

An evaporator airflow fault probability has been calculated for each test case in order to test the effectiveness of the FDD system at identifying evaporator fouling faults. This probability was calculated using Equation (3.32) using the virtual evaporator airflow rate sensor outputs along with the rated airflow for each stage of operation. The results in Figure 4.8 compare test cases at 82 °F ambient conditions where evaporator airflow was normal and reduced to simulate a fouling fault. Fault cases that had reductions in evaporator airflow resulted in high fault probabilities, which can be used to identify faults. In order to assess the sensitivity to ambient temperature, the FDD algorithms were applied to the test cases under 95 °F ambient conditions in Figure 4.9.



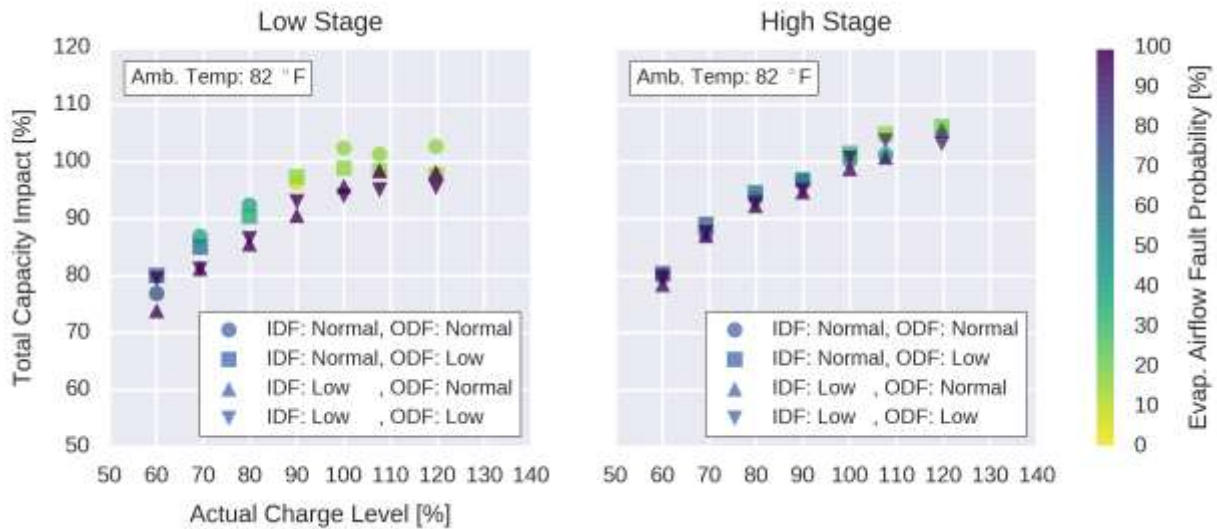


Figure 4.8. The FDD system is able to identify test cases with low evaporator airflow using the statistical fault detection and diagnostics method (System C). Test cases without reductions in evaporator airflow were not identified with high fault probabilities.

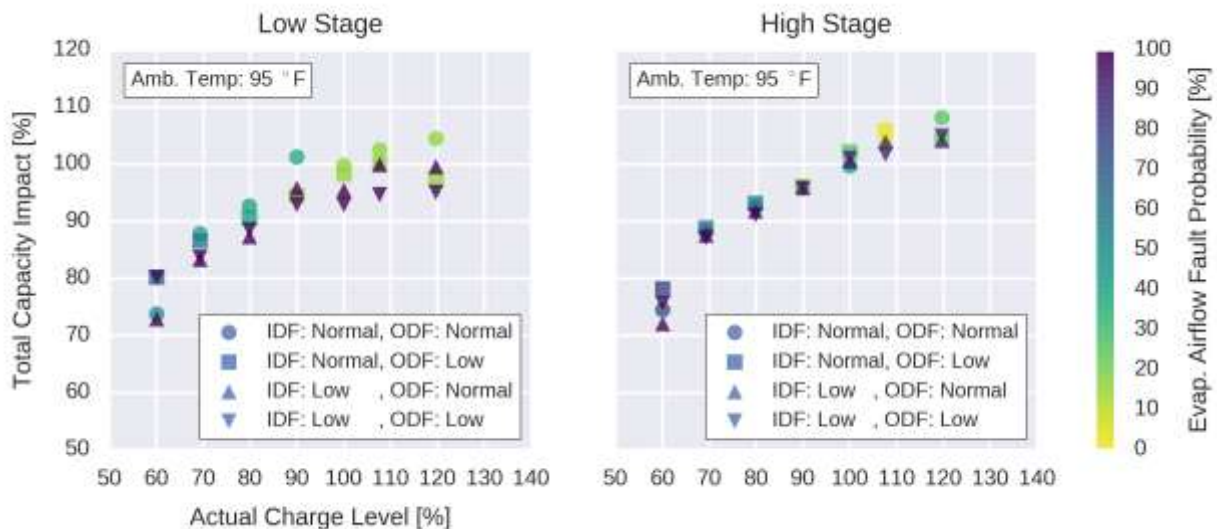


Figure 4.9. The FDD system is able to identify test cases with low evaporator airflow using the statistical fault detection and diagnostics method for test cases under 95 °F outdoor ambient temperature (System C). Test cases without reductions in evaporator airflow were not identified with high fault probabilities.

A condenser airflow fault probability has been calculated for each test case in order to test the effectiveness of the FDD system at identifying condenser fouling faults. This probability was calculated using Equation (3.32) using the virtual condenser airflow rate sensor outputs along with the rated airflow for each stage of operation. The results in Figure 4.10 compare test cases at 82 °F ambient conditions where evaporator airflow was normal and reduced to simulate a fouling fault. Fault cases that had reductions in evaporator airflow resulted in high fault probabilities, which can be used to



identify faults. In order to assess the sensitivity to ambient temperature, the FDD algorithms were applied to the test cases under 95 °F ambient conditions in Figure 4.11.

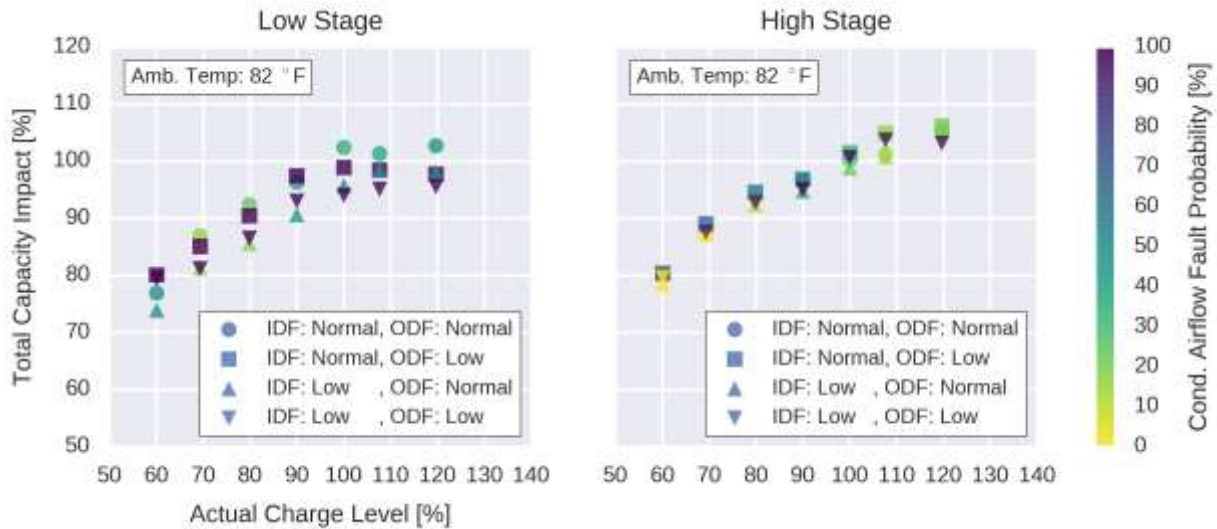


Figure 4.10. The FDD system is able to identify test cases with low condenser airflow using the statistical fault detection and diagnostics method for test cases under 82 °F outdoor ambient temperature (System C). Test cases without reductions in condenser airflow were not identified with high fault probabilities.

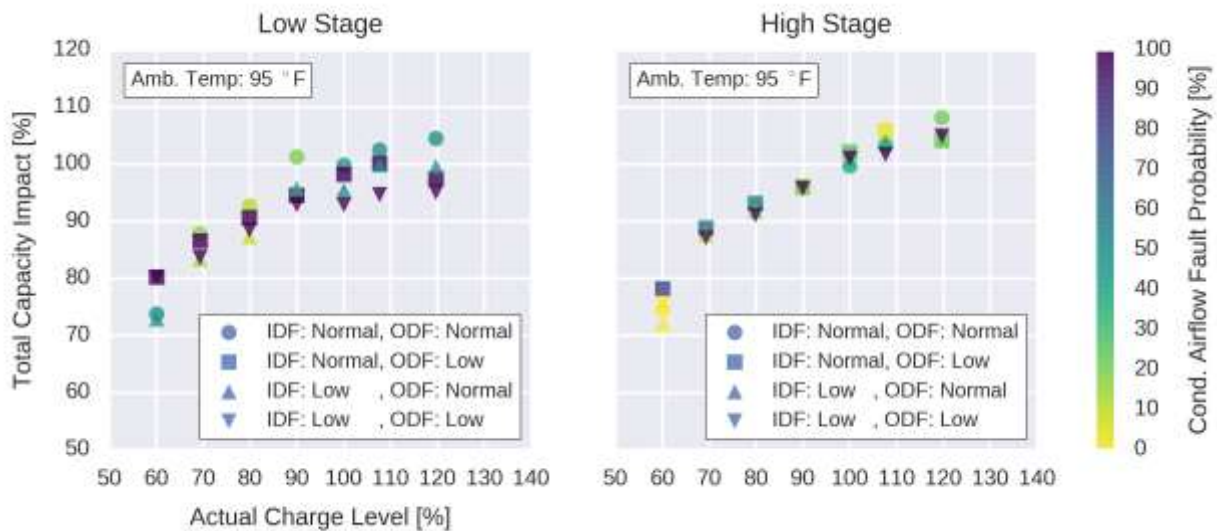


Figure 4.11. The FDD system is able to identify test cases with low condenser airflow using the statistical fault detection and diagnostics method for test cases under 95 °F outdoor ambient temperature (System C). Test cases without reductions in condenser airflow were not identified with high fault probabilities.



The performance of the FDD system at identifying improper charge level faults with respect to impact on COP is shown in Figure 4.12 for tests conducted at 82 °F outdoor temperature. These results show that refrigerant charge faults are identified when significant impacts on COP exist in the system. The results shown in Figure 4.12 also indicate that the FDD system properly identifies improper charge level faults even when low evaporator or condenser airflow faults affect the system simultaneously. The results are reproduced at higher outdoor temperatures (95 °F and 108 °F) in Figure 4.13 and Figure 4.14 respectively.

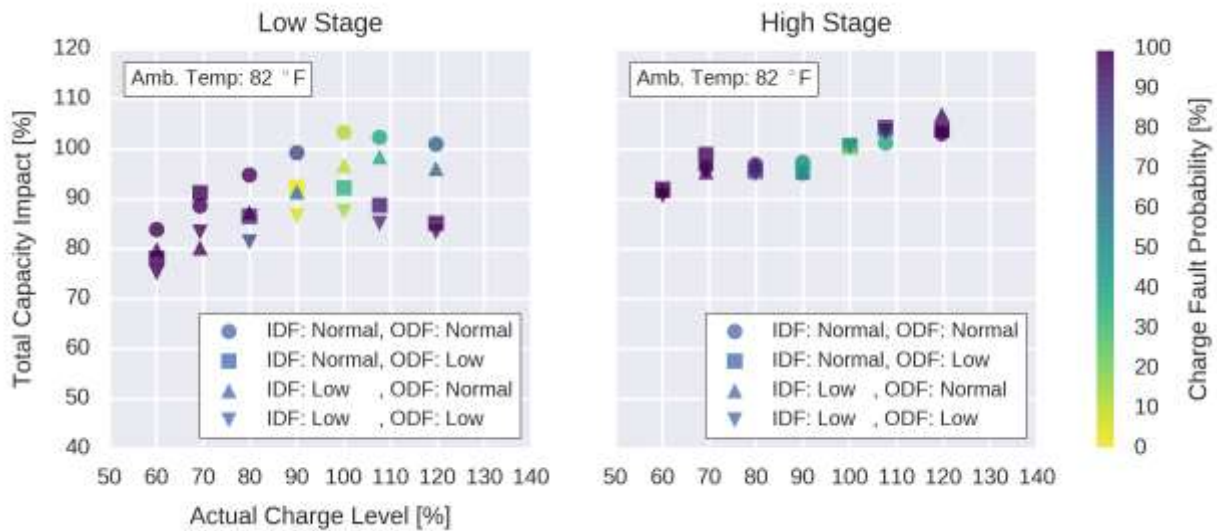


Figure 4.12. Coefficient of performance (COP) impact of refrigerant charge faults at 82 °F outdoor ambient temperature (System C). The points are colored based on the fault probability determined for each test case, indicating faults that have larger impacts are identified with greater probability.



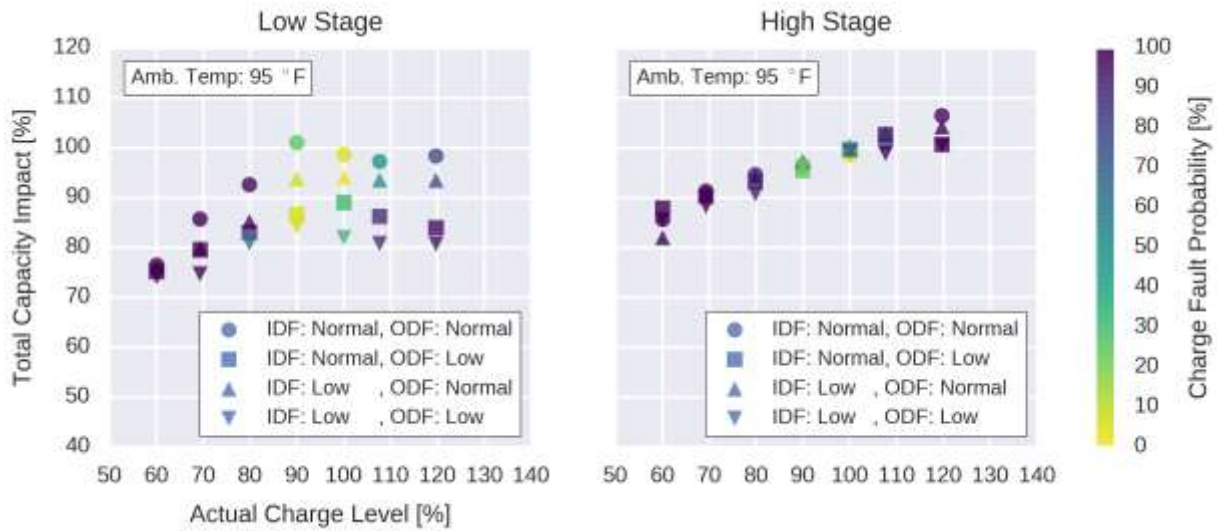


Figure 4.13. Coefficient of performance (COP) impact of refrigerant charge faults at 95 °F outdoor ambient temperature (System C). The points are colored based on the fault probability determined for each test case, indicating faults that have larger impacts are identified with greater probability.

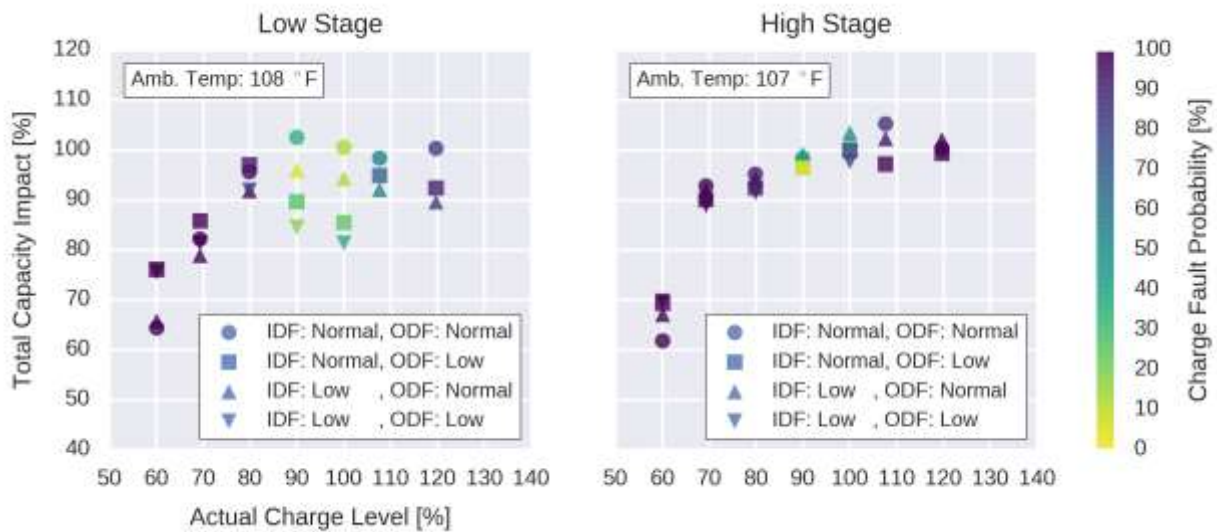


Figure 4.14. Coefficient of performance (COP) impact of refrigerant charge faults at 108 °F outdoor ambient temperature (System C). The points are colored based on the fault probability determined for each test case, indicating faults that have larger impacts are identified with greater probability.



System D: RTU with Finned Tube Condenser and TXV

Following the testing and evaluation of the data collected from System C, the fixed orifice expansion device was replaced with a TXV and the RTU was referenced as System D. The TXV was the original model that was installed on the system when it was received from the original equipment manufacturer. The conditions tested for low and high stage operation are described in Table 4.7 and Table 4.8, respectively.

Table 4.7. Test conditions for RTU with finned-tube condenser and fixed orifice expansion device (System C) for low stage cooling operation in psychrometric test chambers.

Test Variable		Test Values
Compressor Stage	[-]	LOW
Indoor Dry Bulb	[°F]	80
Indoor Wet Bulb	[°F]	57, 67
Outdoor Dry Bulb	[°F]	67, 82, 95, 108
Charge Level ¹	[%]	60, 70, 80, 90, 100, 110, 120
Indoor Fan Torque ²	[%]	30, 60
Outdoor Fan Torque ³	[%]	40, 70

¹ Charge is measured relative to the recommended charge according to the manufacturer’s nameplate data.

² Indoor fan torque is set according to a nominal flow rate of 1350 CFM for low stage operation.

³ Outdoor fan torque is set using the manufacturer’s default value for low stage operation.

Table 4.8. Test conditions for RTU with finned-tube condenser and fixed orifice expansion device (System C) for high stage cooling operation in psychrometric test chambers.

Test Variable		Test Values
Compressor Stage	[-]	HIGH
Indoor Dry Bulb	[°F]	80
Indoor Wet Bulb	[°F]	57, 67
Outdoor Dry Bulb	[°F]	69, 82, 95, 108
Charge Level ¹	[%]	60, 70, 80, 90, 100, 110, 120
Indoor Fan Torque ²	[%]	50, 90
Outdoor Fan Torque ³	[%]	60, 100

¹ Charge is measured relative to the recommended charge according to the manufacturer’s nameplate data.

² Indoor fan torque is set according to a nominal flow rate of 2000 CFM for high stage operation.

³ Outdoor fan torque is set using the manufacturer’s default value for high stage operation.

The accuracy of the VRC model designed for System D for each stage of operation is shown in Figure 4.3 over the range of ambient conditions tested. The performance of the VRC sensor applied to System D was better than System A or System B, which may indicate that a system having a finned tube condenser may be modelled more easily. It was roughly in line with the performance in System C. In both stages of operation, the RMSE was approximately 6.19%. Additionally, the accuracy observed over the range of charge levels was relatively constant – though begins to under predict the charge level for highly overcharged cases.



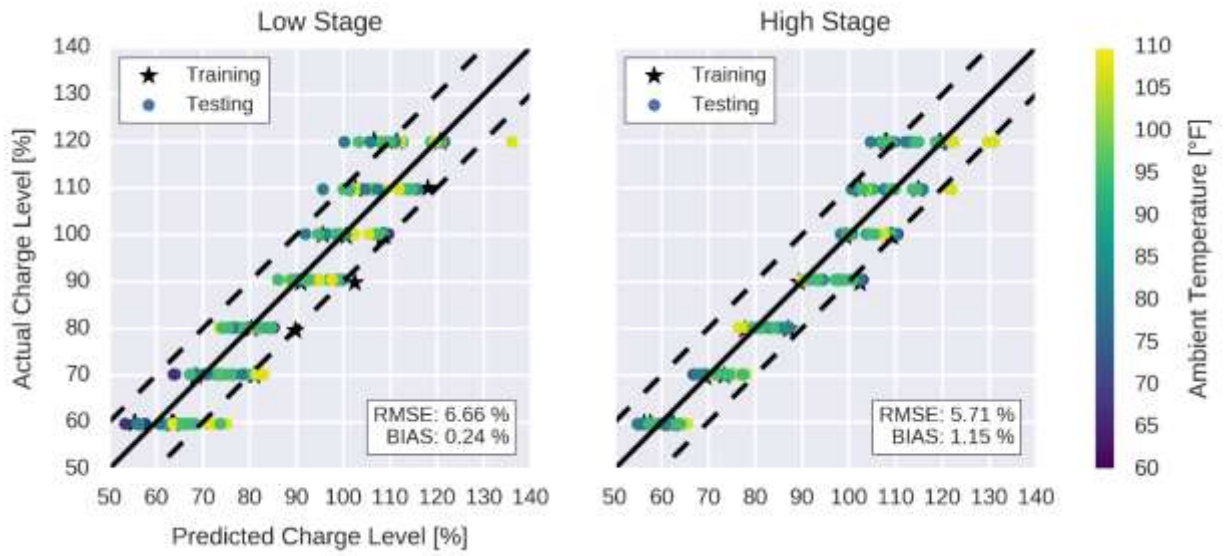


Figure 4.15. Accuracy of VRC sensor developed for System D applied to RTU at range of operating conditions and charge levels.



5 Conclusions

The hardware design for the RTU AFDD system and complete codebase are being made publically available under an open-source license. This will allow equipment manufacturers access to a complete RTU AFDD system that is interoperable with the VOLTRON™ platform with little initial engineering and development effort. Manufacturers can then incorporate this system into their products and make changes where necessary for commercialization. Because the application is open-source, it should encourage equipment manufacturers to further improve the original codebase and hardware design by submitting new features and fixing bugs where present.

Extensive psychrometric chamber testing has been conducted in an effort to assess the performance of a FDD system designed for rooftop units. Testing was performed under a wide range of outdoor and indoor ambient conditions while also injecting combinations of improper refrigerant charge, evaporator airflow reduction, and condenser airflow reduction faults. A statistical method for determining the probability of a fault being present in the system was able to identify improper charge levels, evaporator airflow reduction and condenser airflow reduction. Additionally, tests with multiple faults also showed good fault isolation, especially when impacts on total capacity and COP were significant. This indicates that the FDD system is able to identify problems that may cause significant additional energy consumption.



References

- Air-Conditioning, Heating, and Refrigeration Institute (AHRI). (2004). *Standard for Performance Rating of Positive Displacement Refrigerant Compressors and Compressor Units*. ANSI/AHRI Standard 540. Arlington, VA.
- Akyol, B., Haack, J. N., Carpenter, B. J., Katipamula, S., Lutes, R. G., & Hernandez, G. (2015). *Transaction-Based Building Controls Framework, Volume 2: Platform Descriptive Model and Requirements*. PNNL-24395, Pacific Northwest National Laboratory, Richland, WA.
- Armstrong, P. R., Laughman, C. R., Leeb, S. B., & Norford, L. K. (2006). Detection of Rooftop Cooling Unit Faults Based on Electrical Measurements. *HVAC&R Research*, 12(1), 151-176.
- Cowan, A. (2004). *Review of Recent Commercial Roof Top Unit Field Studies in the Pacific Northwest and California*. New Buildings Institute [NBI] for Northwest Power and Conservation Council [NPCC] and Regional Technical Forum [RTF].
- Dabiri, A. E. & Rice, C. K. (1981) A Compressor Simulation Model with Corrections for the Level of Suction Gas Superheat. *ASHRAE Transactions*, 87(2).
- Hjortland, A. L. & Braun, J. E. (2016). Virtual sensors for rooftop unit air-side diagnostics. *Science and Technology for The Built Environment*, 22(2), pp.189-200.
- Jacobs, P. (2003). *Small HVAC Problems and Potential Savings Reports*. California Energy Commission [CEC].
- Katipamula, S., & Brambley, M. (2005). Methods for Fault Detection, Diagnostics, and Prognostics for Building Systems-A Review, Part I. *HVAC&R Research*, 11(1), 3-25.
- Katipamula, S., & Brambley, M. (2005). Methods for Fault Detection, Diagnostics, and Prognostics for Building Systems-A Review, Part II. *HVAC&R Research*, 11(2), 169-187.
- Katipamula, S., Kim, W., Lutes, R., & Underhill, R. M. (2015). *Rooftop unit embedded diagnostics: Automated fault detection and diagnostics (AFDD) development, field testing and validation*. Pacific Northwest National Laboratory.
- Kim, W. & Braun, J. E. (2012). Evaluation of the impacts of refrigerant charge on air conditioner and heat pump performance. *International Journal of Refrigeration*, 35(7), 1805-1814.
- Kim, W. & Braun, J. E. (2013) Performance evaluation of a virtual refrigerant charge sensor. *International Journal of Refrigeration*, 36(3), 1130-1141.
- Kim W. & Braun, J. E. (2016) Development and evaluation of virtual refrigerant mass flow sensors for fault detection and diagnostics. *International Journal of Refrigeration*, 63(2), 184-198.
- Li, H. & Braun, J. E. (2007). A Methodology for Diagnosing Multiple Simultaneous Faults in Vapor-Compression Air Conditioners. *HVAC&R Research*, 13(2), 369-396.
- Li, H. & Braun, J. E. (2007) Decoupling features and virtual sensors for diagnosis of faults in vapor compression air conditioners. *International Journal of Refrigeration*, 30(3), 546-564.
- Li, H. & Braun, J. E. (2007). Economic evaluation of benefits associated with automated fault detection and diagnosis in rooftop air conditioners. *ASHRAE Transactions*, 113(2), 200.



- Li, H. & Braun, J. E. (2009). Virtual Refrigerant Pressure Sensors for Use in Monitoring and Fault Diagnosis of Vapor-Compression Equipment. *HVAC&R Research*, 15(3), 597-617.
- Najafi, M., Auslander, D., Haves, P., & Sohn, M. (2012). A statistical pattern analysis framework for rooftop unit diagnostics. *HVAC&R Research*, 18(3), 406-416.
- NMR Group, Inc. (2015). *Baseline Characterization Market Effects Study of Investor-Owned Utility Residential and Small Commercial HVAC Quality Installation and Quality Improvement Programs in California (Work Order 054)*. Submitted to California Public Utilities Commission.
- Patil, A., Hjortland, A. L., Braun, J. E., Kurtulus, O., & Horton, W. T. (2016) Development and Evaluation of an Automated Virtual Refrigerant Charge Sensor Training Kit. *International Refrigeration and Air Conditioning Conference*. West Lafayette, IN.
- Rossi, T., & Braun, J. (1997). A Statistical, Rule-Based Fault Detection and Diagnostic Method for Vapor Compression Air Conditioners. *HVAC&R Research*, 3(1), 19-37.
- Somasundaram S., Pratt, R. G. Akyol, B. A., Fernandez, N., Foster, N. A., Katipamula, S., Mayhorn, E. T., Somani, A., Steckley, A. C., & Taylor, Z. T. (2014). *Transaction-Based Building Controls Framework, Volume 1: Reference Guide*. Pacific Northwest National Laboratory, Richland, WA.
- Yuill, D. P. & Braun, J. E. (2013). Evaluating the performance of fault detection and diagnostics protocols applied to air-cooled unitary air-conditioning equipment. *HVAC&R Research*, 19(7), 882-892.



Appendix

A.1 Electronics Schematics

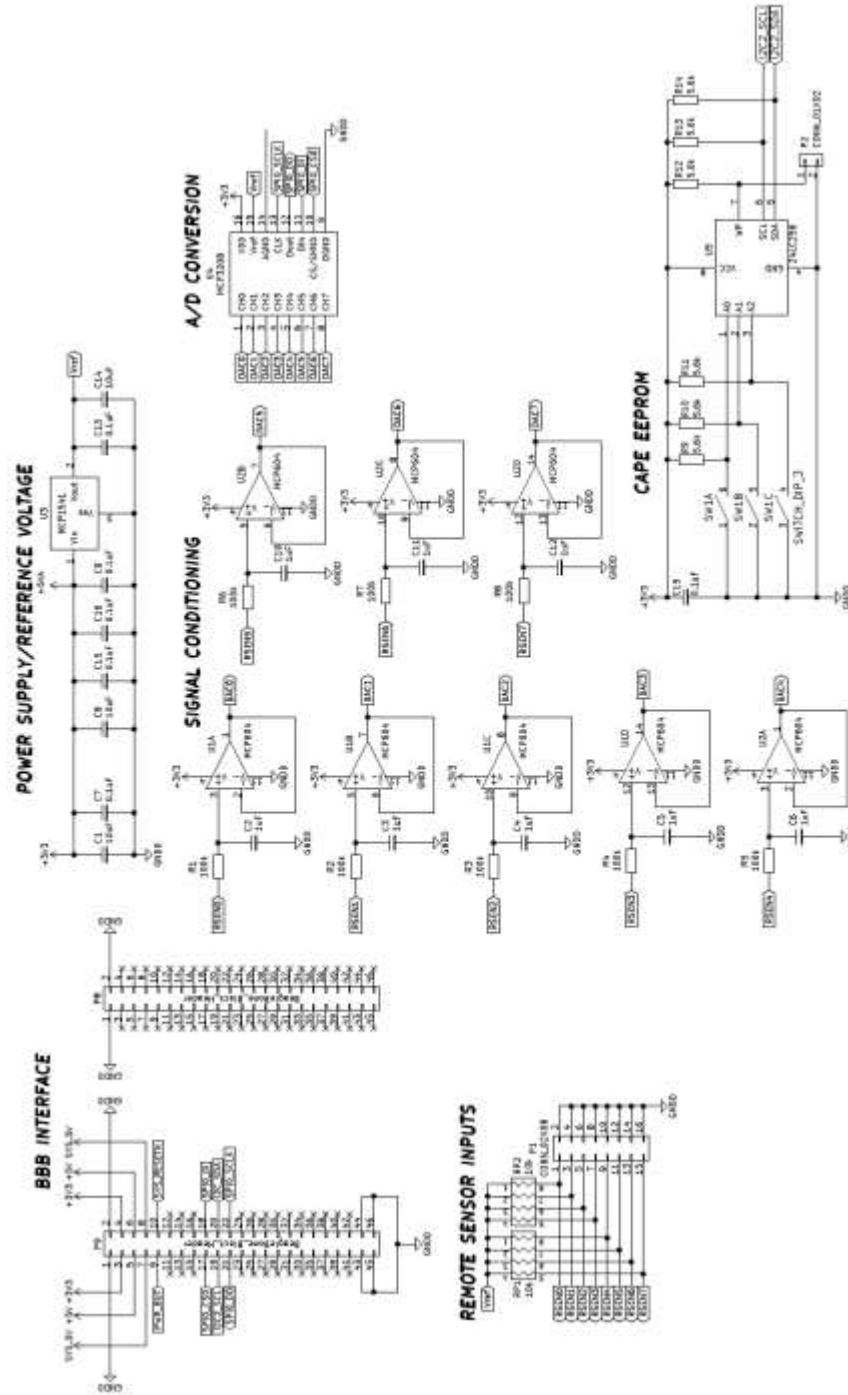


Figure A.1. Electronics schematics of RTU AFDD system.



A.2 Electronics Cost Study

Table A.1. Component cost summary for RTU AFDD prototype including on-board virtual evaporator airflow rate sensor for different number of units manufactured.

Part	Individual Component Price per Quantity Ordered						Quantity Required per Unit	Total Component Cost per Units Manufactured					
	1	10	25	50	100	500		1	10	25	50	100	500
MCP3208	\$4.18	\$3.48	\$2.90	\$2.90	\$2.64	\$2.64	1	\$4.18	\$3.48	\$2.90	\$2.90	\$2.64	\$2.64
MCP604	\$1.25	\$1.04	\$0.86	\$0.86	\$0.78	\$0.78	2	\$2.50	\$2.08	\$1.72	\$1.56	\$1.56	\$1.56
MCP1541	\$0.92	\$0.77	\$0.64	\$0.64	\$0.58	\$0.58	1	\$0.92	\$0.77	\$0.64	\$0.64	\$0.58	\$0.58
R _T	\$6.12	\$4.77	\$3.87	\$3.42	\$3.33	\$3.33	8	\$38.16	\$27.36	\$26.64	\$26.64	\$26.64	\$26.64
R _S	\$0.31	\$0.22	\$0.22	\$0.13	\$0.10	\$0.05	8	\$1.72	\$1.00	\$0.77	\$0.77	\$0.42	\$0.42
HIH6130	\$13.75	\$10.06	\$9.41	\$8.89	\$8.33	\$7.66	3	\$41.25	\$28.24	\$26.67	\$24.99	\$24.99	\$22.98
R ₁	\$0.31	\$0.22	\$0.22	\$0.13	\$0.10	\$0.05	12	\$2.58	\$1.16	\$1.16	\$1.16	\$0.64	\$0.64
R ₂	\$0.37	\$0.26	\$0.26	\$0.15	\$0.11	\$0.06	6	\$2.22	\$0.89	\$0.69	\$0.69	\$0.38	\$0.38
C ₁	\$0.94	\$0.79	\$0.79	\$0.79	\$0.10	\$0.05	15	\$11.87	\$1.48	\$1.48	\$0.76	\$0.76	\$0.76
C ₂	\$0.37	\$0.25	\$0.25	\$0.25	\$0.10	\$0.05	4	\$1.48	\$0.98	\$0.39	\$0.39	\$0.39	\$0.20
C ₃	\$0.49	\$0.34	\$0.34	\$0.34	\$0.20	\$0.15	1	\$0.49	\$0.34	\$0.34	\$0.34	\$0.20	\$0.15
C ₄	\$0.54	\$0.43	\$0.43	\$0.43	\$0.26	\$0.16	3	\$1.62	\$1.28	\$1.28	\$0.77	\$0.77	\$0.49
BBB	\$55.00	\$55.00	\$55.00	\$55.00	\$55.00	\$55.00	1	\$55.00	\$55.00	\$55.00	\$55.00	\$55.00	\$55.00
Total Unit Cost per Units Manufactured:								\$163.99	\$124.06	\$119.68	\$116.61	\$114.97	\$112.44

A.2 RTU AFDD Software Repository

The software and hardware designs for the RTU AFDD system have been posted to a GitHub repository. The code, documentation, and electronics designs, and license information can be downloaded at the following link: https://www.github.com/ahjortland/rtu_afdd_agents/tree/master/RTU_AFDD_AGENT.

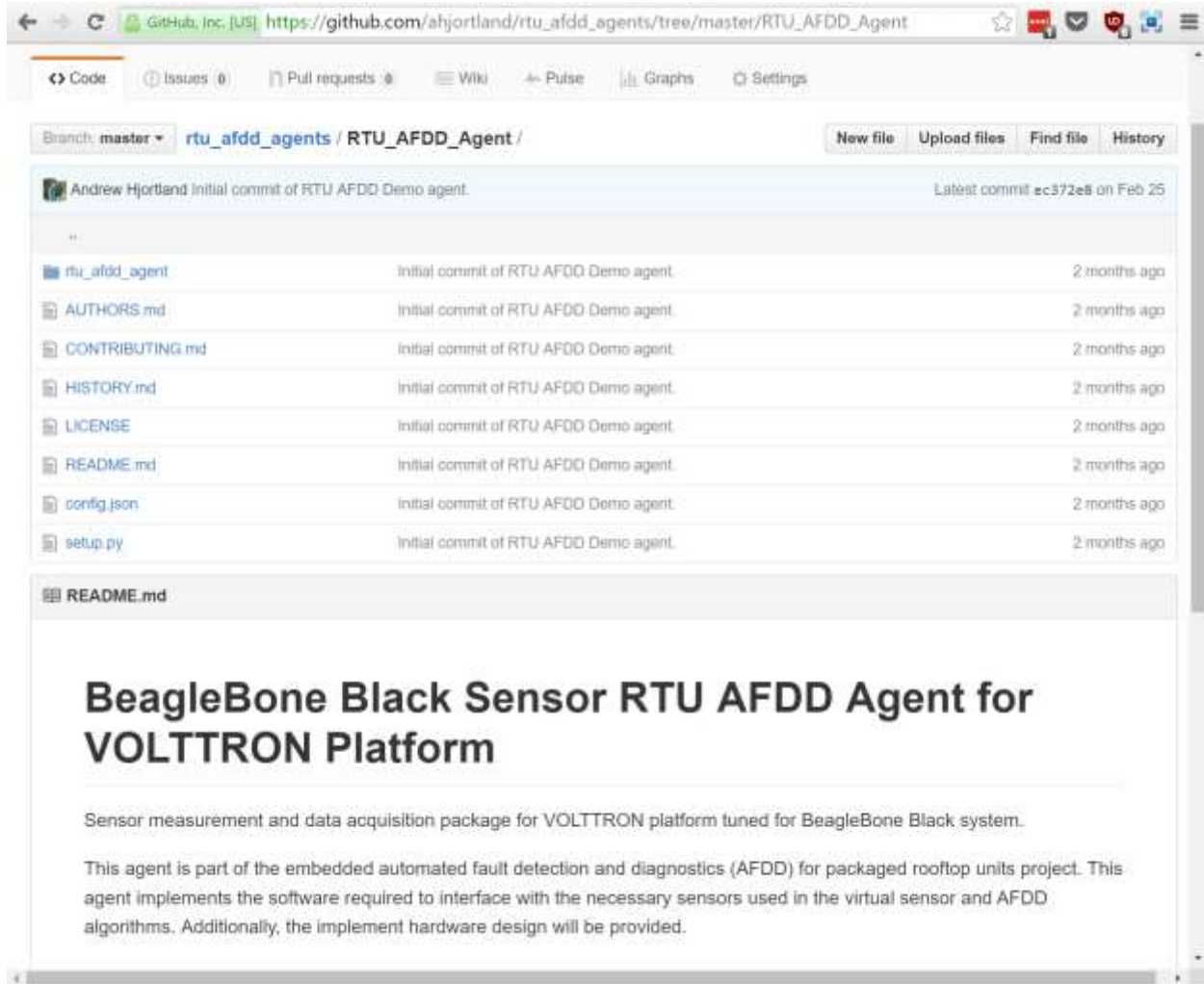


Figure A.2. Screenshot of GitHub repository for RTU AFDD software and hardware designs.